# Late Glacial-Holocene cirque glacier chronology on sub-Antarctic Kerguelen Archipelago (49°S) based on cosmogenic $^{36}$Cl exposure dating

Talin Tuestad [a],[*], Shasta M. Marrero [b], Henriette Linge [a], Philip Deline [c], Ludovic Ravanel [c], Jostein Bakke [a], Fabien Arnaud [c], Andrew S. Hein [d], Delia M. Gheorghiu [e], Richard Shanks [e]

[a] Department of Earth Science and Bjerknes Centre for Climate Research, University of Bergen, Norway
[b] School of Earth and Environmental Sciences, Cardiff University, UK
[c] EDYTEM, Université Savoie Mont Blanc, CNRS, Le Bourget du Lac, France
[d] School of Geosciences, University of Edinburgh, Edinburgh, UK
[e] Scottish Universities Environmental Research Centre, East Kilbride, UK

## ARTICLE INFO

## ABSTRACT

Sub-Antarctic glacier chronologies can provide valuable information about the past variability of climate dynamics in the Southern Ocean region. The Kerguelen Archipelago (49°S) is advantageously located under the influence of the Southern Hemisphere's westerly wind belt, thus fluctuations of climate-sensitive glaciers on Kerguelen can provide a baseline for understanding the behavior of this atmospheric regime in response to climatic forcings. We present 17 $^{36}$Cl exposure ages of moraine and erratic boulders to provide chronological constraints to paleoglacier extents of the Guynemer cirque glacier, located just north of the Cook Ice Cap. Erratic boulders show ice thinning in the Guynemer region started to occur in the Late Glacial by 13.5 ka and continued past 12.4 ka. Ice retreat was punctuated by the formation of two moraine stages, the outermost at 11.5 ± 0.4 ka followed by another at 10.4 ± 1.2 ka, which are indicative of Early Holocene glacier advances/standstills. A glacial advance occurred at 1.4 ± 0.3 ka, which corroborates other Late Holocene re-advances elsewhere on the archipelago. Finally, three undated moraine stages are found between 1.4 ka and the 1960s. The lack of moraines after 10.4 ka and through the Mid-Holocene suggests that the Guynemer glacier was significantly smaller during this extended period of the Holocene compared to its Early Holocene as well as its Late Holocene limits. The Guynemer glacier history provides unique evidence of Early Holocene moraines on Kerguelen, which have not been discovered thus far on the archipelago. Similar to glaciers in Patagonia, New Zealand and South Georgia, the Guynemer glacier was at its largest Holocene extent in the Early Holocene. However, while other southern mid-latitude glacier chronologies show progressively smaller glacial extents throughout the Mid- to Late Holocene, the Late Holocene re-advance of the Guynemer glacier, like other Kerguelen glaciers, likely exceeded its Mid-Holocene extent.

## 2. Introduction

Glaciers in the sub-Antarctic zone, like much of the world, have been experiencing accelerated retreat in past decades in the face of ongoing climatic changes (Gordon et al., 2008; Cook et al., 2014; Favier et al., 2016). A major mechanism behind this recent glacial retreat is the shifting position and strength of the Southern Hemisphere's westerly winds (SHW), which greatly impact global climate through the role they play in driving ocean circulation and ventilation of $CO_2$ from the Southern Ocean (Le Quéré et al., 2007; Hodgson and Sime, 2010;

Sigman et al., 2010; Saunders et al., 2018). The latitudinal variations of the SHW belt are largely regulated by the Southern Annular Mode (SAM), which appertains to pressure differences at sea level between the southern mid-latitudes and Antarctica (Fogt and Marshall, 2020). In recent decades, SAM has moved towards a positive phase with a pole-ward shift of the westerlies, resulting in the dramatic retreat of glaciers in Indian sector of the southern mid-latitudes (Favier et al., 2016). Thus, glacier fluctuations in the sub-Antarctic region can provide valuable insight into the past climate dynamics of the region. While glacial records from Patagonia and New Zealand are relatively abundant, there is

still a lack of knowledge about the past glacial history of the sub-Antarctic regions (Hodgson et al., 2014). The Kerguelen archipelago provides a unique opportunity as the largest glaciated region in the South Indian Ocean, where the scarcity of glacier-covered landmasses has resulted in relatively few paleoclimatic reconstructions (Petherick et al., 2022). Recent studies have used $^{36}$Cl surface exposure dating of glacial landforms on Kerguelen to provide insight into its glacial history

spanning from Marine Isotope Stage 3 (MIS 3) to the last several centuries (Jomelli et al., 2017, 2018; Charton et al., 2020, 2022, 2024). Nonetheless, many questions remain concerning the Holocene glacial history of the archipelago. Thus, the establishment of a robust glacier chronology on Kerguelen can provide a much-needed baseline that can offer valuable insight into past climate dynamics in the Southern Ocean. Here we present 17 new $^{36}$Cl surface exposure ages from the Guynemer
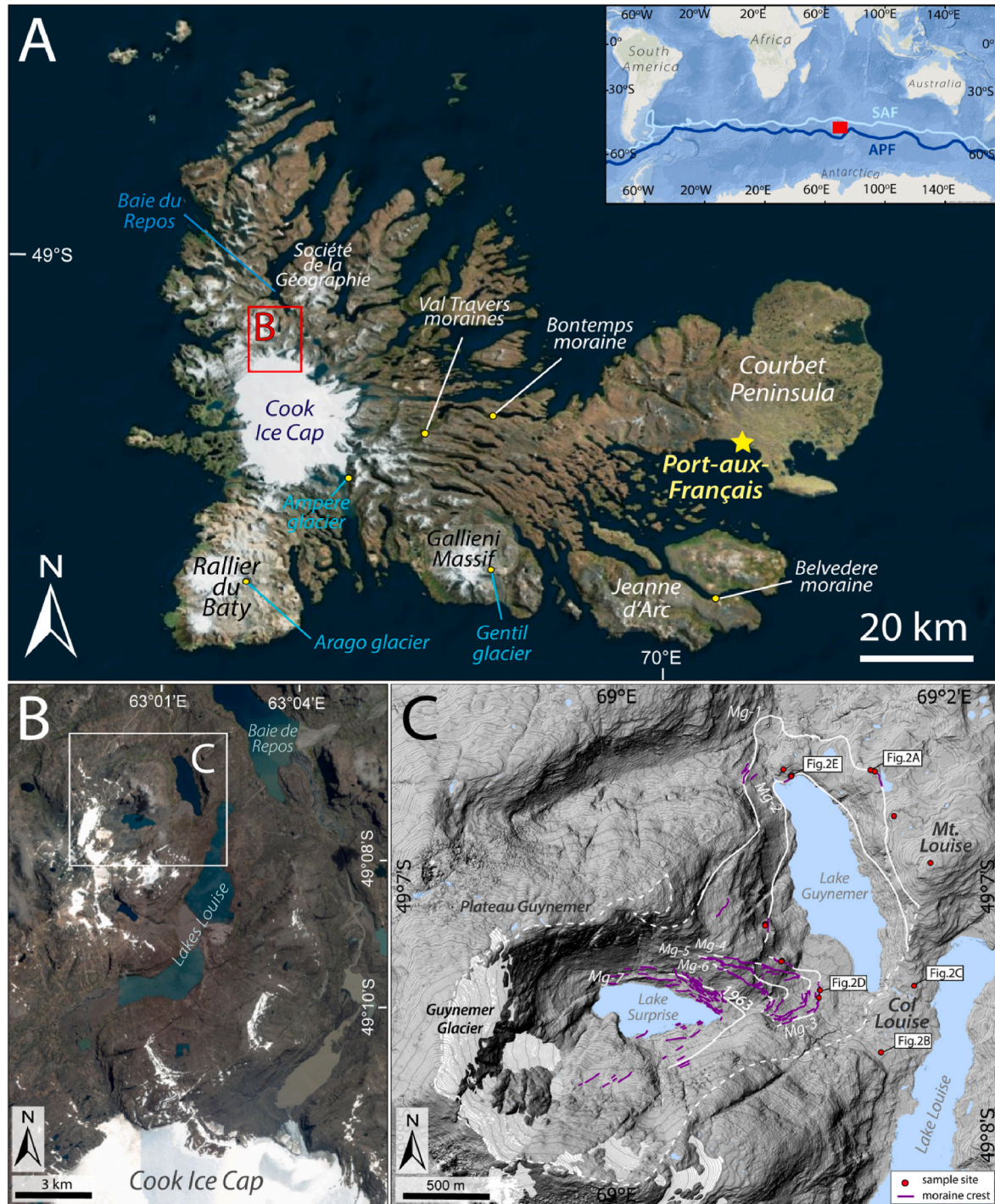


**Fig. 1.** (A) A satellite image of the Kerguelen Archipelago showing site locations mentioned in the text. Red box shows location of Fig. 1B. Satellite image: Landsat 7, November 2001. The inset shows a map of the Southern Ocean highlighting the location of Kerguelen (red box), the sub-Antarctic front (SAF) and the Antarctic Polar Front (APF; Park et al., 2009). (B) Study region north of the Cook Ice Cap. The white box denotes the Guynemer area shown in Fig. 1C. Pléiades orthoimage (2021) retrieved from Bing Aerial. (C) The Guynemer study area showing mapped moraine crests (purple lines) and reconstructed paleoglacier extents (white lines) from Deline et al. (2024). The dotted white line represents the ice divide and red dots reflect sample locations from this study. Locations of field photos in Fig. 2 are outlined by the white boxes. DEM is derived from Pléiades orthoimages.

region just north of the Cook Ice Cap (CIC), which introduce the first age constraints for paleoglacier reconstructions of this region.

## 3. Study area

The sub-Antarctic Kerguelen archipelago (49°S, 69°E), located in the southern Indian Ocean (Fig. 1A), is comprised of the main island Grande Terre and its surrounding *c.* 300 islands, with a total surface area of 7215 km$^2$. The archipelago emerged from the basaltic Kerguelen Oceanic plateau c. 40 Ma ago. The mountainous western region of Kerguelen, characterized by numerous fjords and glacial valleys, is largely occupied by the CIC (1030 m a.s.l.; Fig. 1A), the largest ice body on Kerguelen covering an area of about 400 km$^2$ in 2020 (Verfaillie et al., 2021). Aside from the CIC, local glaciers are also found elsewhere on the archipelago including at base of Mont Ross, the highest peak (1850 m a.s.l.) of the archipelago located on the Gallieni massif south of the CIC, as well as on the peninsulas of Rallier du Baty (reaching 1262 m a.s.l.) and Société de la Géographie (1081 m a.s.l.; Fig. 1A). In contrast, the Courbet peninsula on the eastern sector of Grand Terre is comprised of completely ice-free lower relief terrain (<200 m a.s.l) characterized predominantly by Quaternary deposits. Nonetheless, there is evidence of previous ice cover on the eastern region of Kerguelen as demonstrated by features such as glacial erratics and Rogen moraines (Hall, 1984).

Given the volcanic origin of the archipelago, the bedrock geology of Kerguelen is dominated by up to 900 m thick tholeiitic flood basalts that cover over 80 % of the islands (Gautier et al., 1990). Basalts are locally intruded by various types of plutonic volcanic rocks, such as the quartz-bearing syenites on the Rallier du Baty peninsula and trachyte intrusions on Société de la Géographie peninsula and its surrounding region (Nougier, 1970). In the Société de la Géographie region, younger intrusions formed from 5 to 15 Ma are associated with the alteration of basalts by meteoric and hydrothermal water, resulting in the precipitation of secondary minerals such as clay minerals, zeolites and quartz geodes (Renac et al., 2010). In addition, young trachyte flows are found on the Gallieni massif formed by the stratovolcano Mont Ross.

### 3.1. Climatic setting

The Kerguelen Archipelago is located within the influence of the SHW, the strength and position of which are associated with SAM, which is defined by the mean sea-level pressure gradient between 40°S and 65°S (Fogt and Marshall, 2020). During SAM-positive phases, SHW belt is strengthened and shifts southward towards Antarctica, which results in less precipitation and higher temperatures on Kerguelen (Favier et al., 2016). Conversely, a SAM-negative phase is associated with weaker SHW and a northward shift of the wind belt (Fogt and Marshall, 2020).

Daily temperature and precipitation measurements have been recorded since the 1950s by the weather station at Port-aux-Français on the southern coast of the Courbet peninsula (Fig. 1A). The mean annual temperature is *c.* 4.9 °C (1991–2020), with the mean monthly temperature ranging from 2.2 °C in the winter (July) to 8.2 °C in the summer (February). Due to the strong föhn effect caused by the presence of the CIC to the west, mean annual precipitation in the western region is significantly greater than that of the eastern sector. The east has a mean annual precipitation of 694 mm at PaF (1999–2020), while the west averaged 3155 mm (1995–2001; Verfaillie et al., 2015, 2019).

### 3.2. Previous glacial studies on Kerguelen

Previous studies on the glacial history of Kerguelen have used $^{36}$Cl dating of glacial landforms to produce a general glacial chronology ranging from MIS 3 (~42 ka) to the last several hundred years. a moraine near Port-aux-Français on the Courbet Peninsula has been dated to *c.* 42 ka, demonstrating significant ice cover on Kerguelen during MIS 3 (Fig. 1A; Charton et al., 2024). Ice cover had a more limited extent during the global Last Glacial Maximum compared to that of MIS 3, culminating on the Jeanne d'Arc peninsula and the central part of Kerguelen (Fig. 1A; Charton et al., 2024). General deglaciation occurred after the global Last Glacial Maximum, which was interrupted by glacial advances/standstills during the Late Glacial period, as indicated by several $^{36}$Cl dated moraines that were likely deposited during the Antarctic Cold Reversal (ACR, 14.5–12.9 ka) and/or Henrich Stadial 1 (17.5–14.7 ka; Rasmussen et al., 2014). Such moraines include the Bontemps moraine (13.6 ± 1.5 ka; Fig. 1A; Jomelli et al., 2017, 2018) located 26 km downstream from the current margin of the CIC outlet Explorateur glacier, as well as the V1 (16 ± 1.9 ka) and V2 (12.9 ± 1.7 ka) moraines in the Val Travers valley (Fig. 1A; Charton et al., 2022). Glaciers similarly recorded Late Glacial advances as shown by the Belvedere moraine (15.5 ± 1.8 ka; Fig. 1A; Jomelli et al., 2017, 2018) formed by a local glacier on the Jeanne d'Arc peninsula, the G1 moraine of the debris-covered Gentil glacier (14.3 ± 2.3 ka; Fig. 1A; Charton et al., 2020) on the Gallieni massif, and the A1 moraine (13.6 ± 1.8 ka; Charton et al., 2022) deposited by the Arago glacier on the Rallier du Baty peninsula (Fig. 1A).

The existing $^{36}$Cl chronology shows a lack of glacial fluctuations in the Early to Mid-Holocene (11.7 ka – 4.3 ka; Walker et al., 2019). Recent retreat of the CIC outlet Ampere glacier (Fig. 1A) exposed peat deposits on the eastern margin of the glacier at two distinct elevations (60 and 150 m a.s.l.), which were radiocarbon dated to 13.1–11.2 cal ka BP and 5.0–5.2 cal ka BP (Frenot et al., 1997). Given that the exposed sites must have been ice-free to allow the deposition of peat, the glacial front at the time of peat formation must have been upstream of the peat deposits, which suggests that glacial extent during the Mid-Holocene may have been smaller than during the Late Holocene when glaciers re-advanced (Frenot et al., 1997; Jomelli et al., 2017; Charton et al., 2020).

$^{36}$Cl dating of moraines of the Ampere glacier suggests that there were potentially two advances in the last millennium: an older advance at 1.0 ± 4.7 ka and a subsequent one at 480 ± 290 a (Verfaillie et al., 2021; Charton et al., 2022). A Late Holocene advance may also be found at the Gentil glacier, whose G2 moraine yielded a mean age of 2.62 ± 0.97 ka (Charton et al., 2020). Similarly, the Arago glacier seems to have also experienced two glacial advances in the last millennium as recorded by the A2a moraine (1.1 ± 0.3 ka) and the younger A2b moraine (300 ± 170 a; Charton et al., 2022).

Several recent studies have demonstrated that the CIC has been experiencing dramatic glacial retreat since the 1960s (*i.e.* Berthier et al., 2009; Favier et al., 2016). Favier et al. (2016) used a mass balance model constrained by long-term glacio-meteorological dataset since the 1950s to show that the CIC has experienced particularly high ice wastage since the 2000s. The high retreat rate has been attributed to atmospheric drying at Kerguelen caused by a southward shift of the Southern Hemisphere's westerlies over the last few decades expressed by the positive index of the SAM (Verfaillie et al., 2015; Favier et al., 2016). Most recently, a reconstruction of glacier dynamics of eight glaciers in northeastern sector of the CIC since the 1960s has shown that the total surface area of the studied glaciers in 2019 had decreased to only 56 % to that of 1962 (Deline et al., 2024).

### 3.3. Study area: the Guynemer region

The Guynemer massif comprises an 18 km$^2$ basaltic stratovolcano located between the CIC and the Baie du Repos that formed *c.* 3.5–1.0 Ma ago (Nougier, 1970). Located in the upper Guynemer basin, the Guynemer cirque glacier has an area of 0.7 km$^2$ with a front currently resting at 340 m a.s.l. (Fig. 1C). The upper basin is also occupied by a 0.25 km$^2$ lake, which recently formed due to the major retreat of glaciers in the region since the 1960s, which has been documented by historical aerial photos (Deline et al., 2024 and references therein). The lake is not present on historical maps or photos and was discovered during recent fieldwork in 2014, thus is hereby referred to as Lake Surprise. Lake Surprise flows into the lower Guynemer basin occupied by Lake Guynemer (0.65 km$^2$, 90 m maximum depth; Deline et al., 2024), which

drains through a braided river into the Baie du Repos fjord to the north (Fig. 1B). A large delta fan has been formed by sediment supplied from the drainage of Lake Surprise into the southwest portion of Lake Guynemer (Figs. 1C, Fig. 2D–E, Fig. 3A). Like other regions of Kerguelen, the

Guynemer area shows definitive evidence of previous ice cover demonstrated by moraines, erratic boulders, glacially scoured bedrock, and discontinuous cover of till deposits.

Deline et al. (2024) introduced the first investigation of glacial
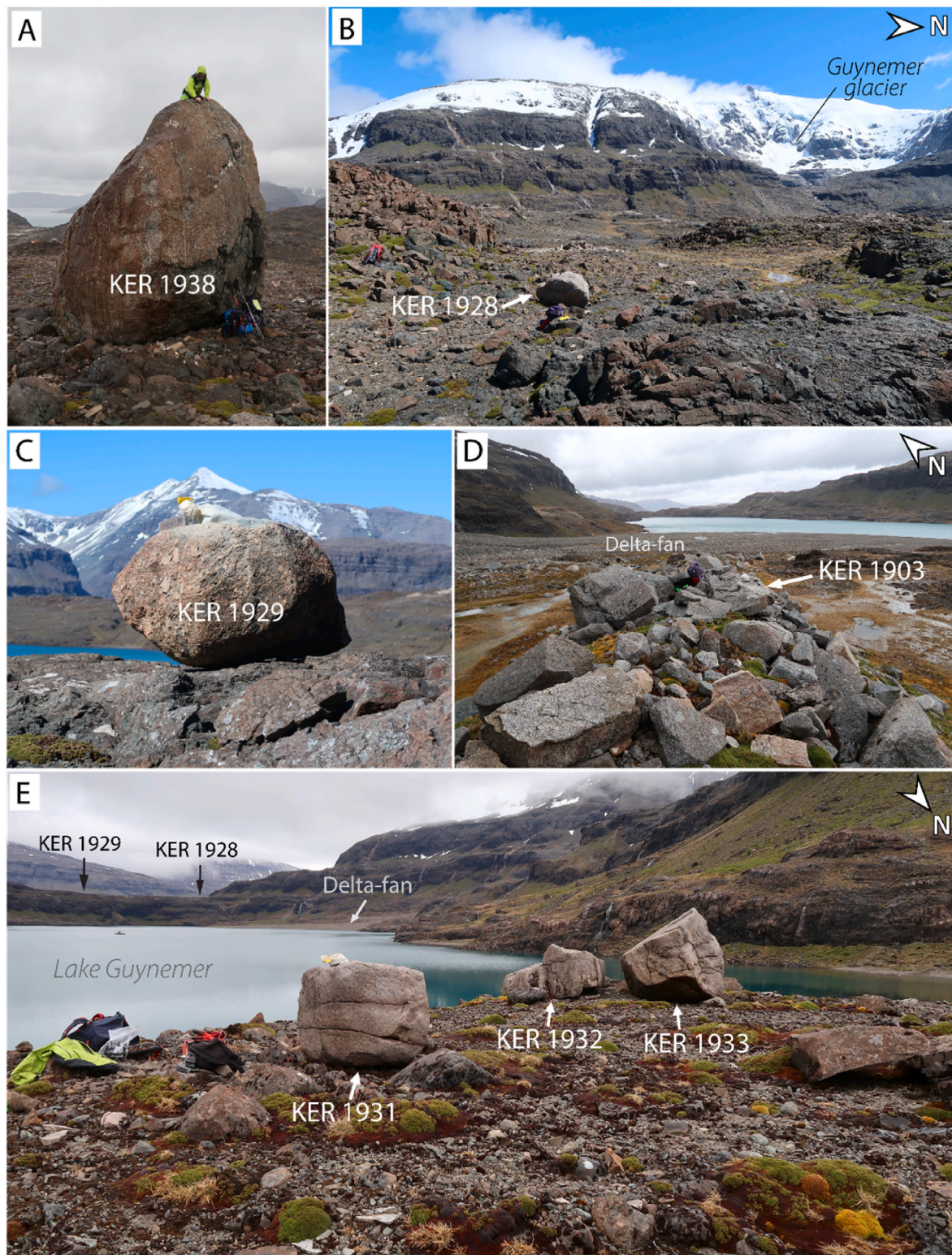


**Fig. 2. (A)** Field photo of boulder KER 1938 from moraine Mg-1. **(B)** Erratic boulder KER 1928 sitting on Col Louise with the Guynemer cirque and glacier shown in the distance on the right. **(C)** Erratic boulder KER 1929 sitting on bedrock on Col Louise. **(D)** Mg-3 moraine ridge with moraine boulder KER 1903. Delta fan shown in the distance feeding into Lake Guynemer. **(E)** Mg-2 moraine on the northern shore of Lake Guynemer with moraine boulders KER 1931, KER 1932; KER 1933. Col Louise is shown in the distance with arrows pointing to the locations of erratic samples KER 1928; KER 1929 shown in (B) and (C), respectively.
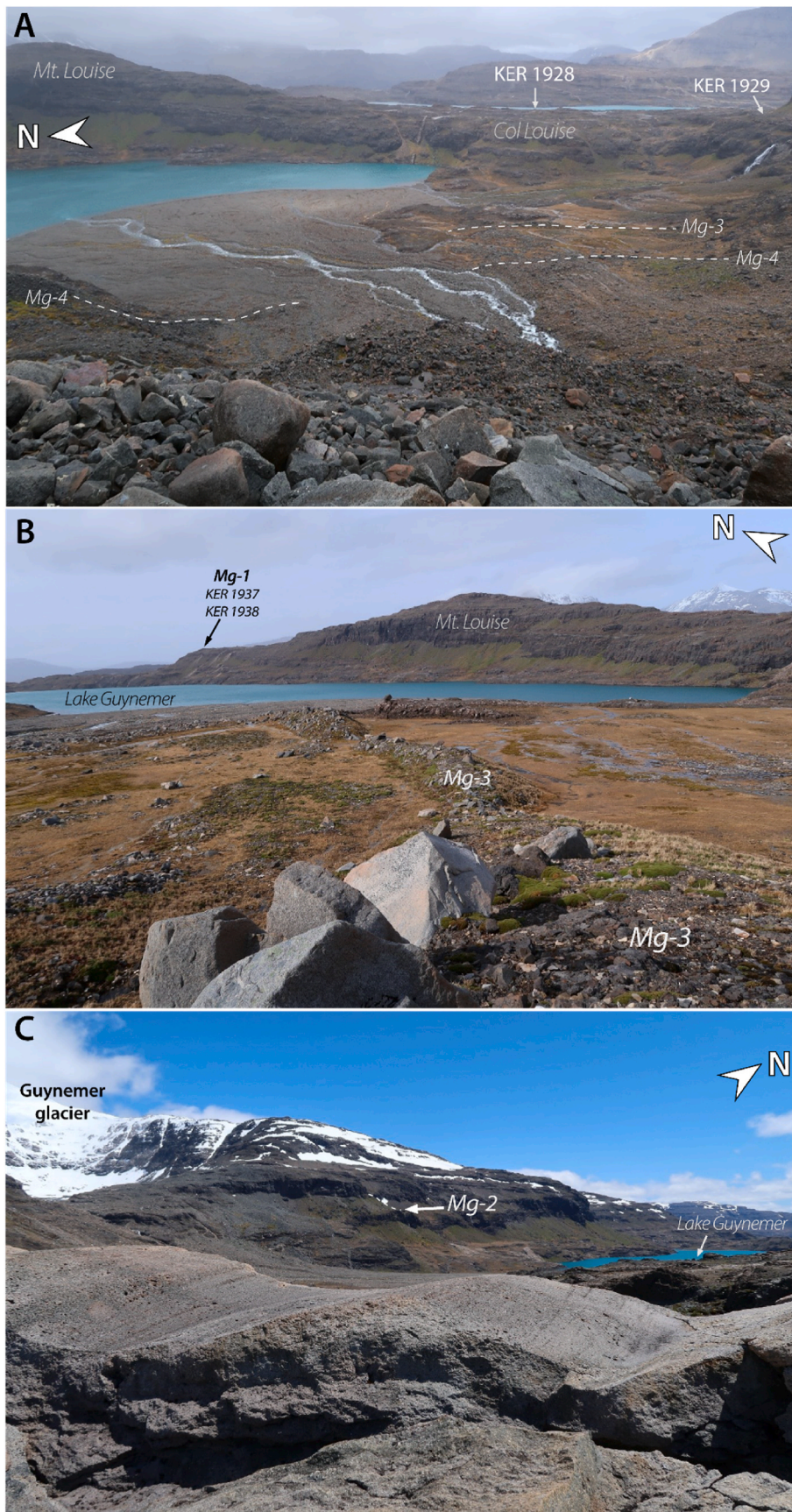
*(caption on next page)*

**Fig. 3.** **(A)** Southeast-ward view of delta-fan formed at the southwest shore of Lake Guynemer. Col Louise and Lake Louise shown in the distance. Moraine ridges belonging to Mg-3 and Mg-4 are outlined by the white dashed lines. **(B)** Northeast-ward view of Mg-3 moraine. Delta-fan and Lake Guynemer shown in the distance with Mt. Louise in the background. **(C)** Northwest view of glacial striations on roches moutonnées on Col Louise showing ice flow between the Guynemer and Louise regions. The position of the Mg-2 lateral moraine is highlighted.

landforms and paleo-glacier reconstruction from the region northeast of the CIC. Moraines of eight local and CIC outlet glaciers were extensively mapped using a multi-method approach including field data, remote sensing, and aerial and satellite imagery to reconstruct paleo-glacier extents up to the 1960s and produced detailed time-slices of glacier retreat from 1960 to 2019. Seven moraine stages have been mapped as part of the Guynemer morainic complex, ranging from the oldest, Mg-1, to the youngest, Mg-7 (Fig. 1C; Deline et al., 2024). Mg-1 is represented by a moraine located around 100 m northeast of Lake Guynemer, along with several moraine segments located near the NW corner of the lake (Fig. 1C). Mg-2 comprises a frontal moraine on the northern shore of Lake Guynemer as well as two matrix-supported lateral moraines with matrix-supported till. During the Mg-1 and Mg-2 extents, the Guynemer glacier occupied the lower Guynemer basin. Mg-3 (Fig. 3A and B) is the outermost of the upper basin moraines, followed by the successively younger Mg-4, Mg-5, and Mg-6. Mg-7 reflects the 1963 extent supplemented by a dozen glacier front positions since the 1960s. Like other glaciers on Kerguelen, the Guynemer glacier experienced accelerated retreat since the 1960s, and has lost around 74 % of its total surface area in the period 1962–2019 (Deline et al., 2024).

## 4. Methods

### 4.1. Sampling

During a field expedition to Kerguelen in November and December 2019, rock samples were collected for $^{36}$Cl exposure dating from moraine boulders and erratic boulders around Lake Guynemer (Figs. 1C and 3; Table 1). During sampling, particular attention was paid to selecting the most suitable boulders available with respect to boulder size and geometry, degree of erosion, boulder/landform stability, and away from slopes to avoid potential rockfall debris following best field sampling practice outlined by Darvill (2013). Samples were collected from the top 2–4 cm of boulders using a rock saw, hammer, and chisel. Topographic shielding was measured using a compass and clinometer and geographic coordinates and elevation were recorded with a hand-held satellite GPS and were later confirmed using a Pléiades-derived digital elevation model. Sample data are outlined in Table 1.

### 4.2. Chlorine-36 analysis

#### 4.2.1. Preparation of targets for $^{36}$Cl analysis
Seventeen samples were processed for $^{36}$Cl analysis by Accelerated Mass Spectrometry (AMS). Four samples were processed as whole-rock and the remaining thirteen samples were processed as feldspar-rich mineral concentrates (Table 1).

The sample preparation for in situ $^{36}$Cl was initiated at the University of Bergen's cosmogenic nuclide preparation facility. All samples were crushed and sieved to a grain size of 250–500 μm. Bulk rock aliquots were taken and sent for major and trace element analysis at Activation Laboratories Ltd. (Actlabs), Ontario, Canada using ICP-OES and ICP-MS (Table 2). Due to complex issues concerning sample composition and low-energy production pathways from $^{35}$Cl, uncertainties in the method are higher for samples with high Cl-content (Schimmelpfennig et al., 2009; Marrero et al., 2016b.) Thus, bulk rock compositions were measured for all samples with higher Cl-content (>10 ppm). Considering the negligible effect of bulk rock compositions on low-Cl-samples (<10 ppm), we measured bulk rock composition for select representative samples which were then substituted for the composition of remaining low-Cl samples of the same lithology. Bulk rock compositions

were used to determine sample lithologies (Table 1) based on "TAS", or total alkali ($Na_2O + K_2O$) vs. silica ($SiO_2$) %, classification of igneous rocks after Le Maitre (1989). Sample lithologies were additionally verified by thin-section analysis. Sample treatment procedure prior to dissolution is provided in Appendix A.

Sample dissolution and $^{36}$Cl target preparation was conducted at the University of Edinburgh's Cosmogenic Nuclide Laboratory. A detailed outline of the laboratory procedure is provided in Appendix A. Targets were sent to the Scottish Universities Environmental Research Centre (SUERC) where $^{36}$Cl/$^{35}$Cl and $^{35}$Cl/$^{37}$Cl ratios were measured by AMS at the SUERC AMS Laboratory (Table 4). AMS results were used to calculate Cl and $^{36}$Cl concentrations by isotope dilution using a $^{36}$Cl data reduction spreadsheet produced by SUERC's Cosmogenic Isotope Analysis Facility that is based on equations published by Wilcken et al. (2013).

#### 4.2.2. $^{36}$Cl exposure age calculations
$^{36}$Cl exposure age calculations were performed using CRONUScalc 2.3, a MATLAB -based exposure age calculator developed by Marrero et al. (2016a). CRONUScalc is similar to the $^{26}$Al/$^{10}$Be calculator by Balco et al. (2008), but is applicable to many of the most commonly used nuclides for surface exposure dating, including $^{36}$Cl. The flux-based LSDn scaling model ('SA'), a nuclide-dependent version of the Lifton-Sat-Dunai model (LSD; Lifton et al., 2014), was used for all age calculations. A bulk density of 2.4 g cm$^{-3}$ was applied to all samples. The following production rates from Marrero et al. (2021) were used in age calculations: 55.6 ± 4.2 atoms $^{36}$Cl (g Ca)$^{-1}$ yr$^{-1}$ for Ca spallation, 156 ± 12 atoms $^{36}$Cl (g K)$^{-1}$ yr$^{-1}$ for K spallation, and 714 ± 191 neutrons (g air) yr$^{-1}$ for the production rate of epithermal neutrons from fast neutrons in the atmosphere at the rock surface.

Recent updates to CRONUScalc 2.3 allow for the input of a rock formation age for each sample rather than assuming the samples are in radiogenic equilibrium with their U and Th concentrations (Anjar et al., 2021). Nonetheless, since the formation age of the samples in this study are relatively old (ranging from 27 to 10 Ma; Table 1) and have relatively low concentrations of U and Th (Table 2), the rock formation age did not affect the surface exposure age of the samples.

The presented $^{36}$Cl ages are not corrected for erosion or snow cover. The study area exhibits a very active surface environment with strong lithology-dependent weathering and erosion rates due to the highly variable geochemical composition of the basalts and the associated intrusions. While quantitative erosion rates are not currently available for Kerguelen, evidence of bedrock erosion is demonstrated by boulders on bedrock pedestals, which suggest the erosion of c. 2–5 cm in the past 10 ka. Nonetheless, an erosion rate of 2 mm kyr$^{-1}$ yields a difference in age of less than 2% for the oldest samples and a difference of less than 1 % for the youngest, which is well-within the uncertainties of the presented $^{36}$Cl ages. Consequentially, any considerations for erosion do not impact the conclusions drawn from the dating results. Similar corrections for snow cover are also considered negligible.

Calculated $^{36}$Cl ages are outlined in Table 4, with both their analytical uncertainties and total uncertainties (analytical + production rate uncertainties). Individual ages are reported with their analytical uncertainties in the text to allow for internal comparison. Moraine ages are presented as weighted arithmetic mean of an age population each with their propagated total uncertainties to allow for external comparison with climatic records (Table 4). Potential outliers from an age population from a single landform were identified through a Chi$^2$ test and were not included in the mean age calculation of the landform. Probability density curves are plotted using analytical uncertainties to

**Table 1**
Geographic location and attributes of samples. Sample lithology is based on Lithology: TB = trachybasalt, B = basalt, BTA = basaltic trachyandesite, T = trachyte, VB = volcanic breccia. Surface type: MB = moraine boulder, E = erratic. Mineral used for dating: WR = whole rock, MS = mineral separates, specified as feldspar-rich mineral concentrates in text.

| Sample name | Latitude (°S) | Longitude (°E) | Elevation (m) | Atm. pressure (hPa) | Topographic shielding factor | $\lambda_{f,e}$ | Thickness (cm) | Lithology | Formation age | Surface type | Moraine set[c] | Material used for dating |
|---|---|---|---|---|---|---|---|---|---|---|---|---|
| KER 1903 | −49.1241 | 69.0206 | 112 | 985.3 | 0.9872 | 152.1 | 2.25 | TB | 10 ± 5 Ma[a] | MB | Mg-3 | MS |
| KER 1905 | −49.1236 | 69.0207 | 106 | 985.6 | 0.9892 | 152.1 | 1.5 | TB | 10 ± 5 Ma[a] | MB | Mg-3 | MS |
| KER 1906 | −49.1216 | 69.0168 | 169 | 978.1 | 0.9818 | 152.1 | 1.25 | TB | 10 ± 5 Ma[a] | MB | Mg-3 | MS |
| KER 1907 | −49.1217 | 69.0168 | 172 | 977.8 | 0.9869 | 152.1 | 1 | B | 27 ± 1 Ma[b] | MB | Mg-3 | WR |
| KER 1911 | −49.1192 | 69.0151 | 185 | 977.2 | 0.9603 | 152.1 | 3.75 | BTA | 10 ± 5 Ma[a] | MB | Mg-2 | MS |
| KER 1912 | −49.1192 | 69.0151 | 184 | 977.0 | 0.9603 | 152.1 | 1.25 | BTA | 10 ± 5 Ma[a] | MB | Mg-2 | MS |
| KER 1913 | −49.1193 | 69.0151 | 190 | 976.6 | 0.9618 | 152.1 | 0.75 | BTA | 10 ± 5 Ma[a] | MB | Mg-2 | MS |
| KER 1928 | −49.1233 | 69.0303 | 151 | 980.3 | 0.9955 | 152.2 | 3 | T | 10 ± 5 Ma[a] | E | – | MS |
| KER 1929 | −49.1278 | 69.0269 | 159 | 979.3 | 0.991 | 152.1 | 2 | VB | 10 ± 5 Ma[a] | E | – | MS |
| KER 1931 | −49.1092 | 69.0178 | 89 | 987.5 | 0.9902 | 152.1 | 1.5 | T | 10 ± 5 Ma[a] | MB | Mg-2 | MS |
| KER 1932 | −49.1093 | 69.0178 | 95 | 987.6 | 0.9902 | 152.1 | 2 | T | 10 ± 5 Ma[a] | MB | Mg-2 | MS |
| KER 1933 | −49.1093 | 69.0178 | 95 | 987.6 | 0.9902 | 152.1 | 2.5 | T | 10 ± 5 Ma[a] | MB | Mg-2 | MS |
| KER 1934 | −49.1093 | 69.0178 | 117 | 985.2 | 0.9947 | 152.1 | 2 | T | 10 ± 5 Ma[a] | E | – | MS |
| KER 1937 | −49.1089 | 69.0259 | 194 | 976.1 | 0.999 | 152.2 | 1.75 | T | 10 ± 5 Ma[a] | MB | Mg-1 | MS |
| KER 1938 | −49.1090 | 69.0263 | 194 | 976.1 | 0.9991 | 152.2 | 2.25 | B | 27 ± 1 Ma[b] | MB | Mg-1 | WR |
| KER 1939 | −49.1119 | 69.0282 | 216 | 972.1 | 0.9988 | 152.2 | 1.5 | B | 27 ± 1 Ma[b] | E | – | WR |
| KER 1940 | −49.1151 | 69.0320 | 278 | 966.2 | 0.9993 | 152.3 | 1.75 | B | 27 ± 1 Ma[b] | E | – | WR |

[a] Renac et al. (2010).
[b] Annell et al. (2007).
[c] Moraine names are introduced in Deline et al. (2024).

allow for internal comparison (Fig. 5, Table 4).

### 4.2.3. $^{36}Cl$ age calculation method of this study vs. that of previous studies on Kerguelen

$^{36}$Cl age calculation in this study employs a different method with different scaling than many of the previously published $^{36}$Cl ages from Kerguelen, which were calculated with the Excel® spreadsheet published by Schimmelpfennig et al. (2009) using the time-invariant "St" scaling model (Stone, 2000). Calculation of $^{36}$Cl ages in this study using "St" scaling produces ages that are less than 5 % older than calculations with "LSDn" scaling. Moreover, different $^{36}$Cl production rates were used in this study compared to most previous studies (Appendix C). We recalculated our $^{36}$Cl ages in the Schimmelpfennig et al. (2009) spreadsheet and substituted our study's CRONUScalc production rates for those used by previous studies (Table C1). These calculations yield $^{36}$Cl ages that are 1–4% older for the older ages and 7–9 % older for the younger ages, which are within the total uncertainties of the presented $^{36}$Cl ages. We also recalculated our ages using the Schimmelpfennig et al. (2009) spreadsheet keeping constant the production rates used by CRONUScalc (Table C1) to identify any differences in calculated results inherent to the calculators themselves, which yielded differences of less than 5%. These minor differences in age results between the two calculators are attributed to differences in the calculation of scaling factors and do not impact the interpretation of results.

## 5. Results

Of the seven moraine stages mapped in the Guynemer moraine complex, the three outermost moraines Mg-1, Mg-2 and Mg-3 have been sampled (Fig. 4). Detailed descriptions of mapped moraines are outlined in Deline et al. (2024).

### 5.1. $^{36}Cl$ ages from Mg-1 moraine boulders (n = 2)

Mg-1 is the outermost mapped extent of the Guynemer glacier and is based on a lateral moraine deposited 100 m above and just east of Lake Guynemer (Figs. 3B and 4; Deline et al., 2024). Several undated lateral moraines deposited 400 m west of lake's outlet have also been correlated with the Mg-1 extent (Fig. 4; Deline et al., 2024). Two moraine boulders KER 1937; KER 1938 (1 m- and 5 m-high, respectively; Fig. 2A) were sampled from the outermost extent of the boulder-rich till associated with Mg-1. KER 1937 and KER 1938 yielded the ages 11.1 ± 0.3 ka and 11.8 ± 0.3 ka, respectively, giving a weighted mean age of 11.5 ± 0.4 ka for Mg-1 (Figs. 4 and 5).

### 5.2. $^{36}Cl$ ages from Mg-2 moraine boulders (n = 6)

Geomorphological mapping by Deline et al. (2024) correlates the Mg-2 terminal moraine on the northern shore of Lake Guynemer with a lateral moraine located further upstream on the western slope of Lake Guynemer (Figs. 3C and 4). Thus, a total of six boulders were sampled from Mg-2: three from the frontal moraine and three from a lateral moraine. The Mg-2 frontal moraine boulders KER 1931, KER 1932; KER 1933 are resting on the ridge surface proximal to one another (Fig. 2E) and yield ages 9.5 ± 0.3 ka, 10.7 ± 0.4 ka, and 8.3 ± 0.3 ka, respectively. The sub-rounded boulders KER 1911, KER 1912; KER 1913 which are marginally embedded in the lateral moraine surface yield ages 11 ± 0.9 ka, 10 ± 0.6 ka and 10.7 ± 0.5 ka, respectively. Based on the Chi$^2$ test conducted on the six resulting ages to identify outliers, samples KER 1933 (8.3 ± 0.3 ka) and KER 1931 (9.5 ± 0.3 ka) have been deemed "too young" to belong to the same age population. Moraine boulder KER 1931 shows no evidence of post-depositional exhumation or surface weathering that would explain a young apparent age. However, sample KER 1933 was taken near the top crest of the boulder (Fig. 2E), thus its younger apparent age may be explained by reduced $^{36}$Cl production proximal to the boulder edge (Masarik and Wieler, 2003). Given the

**Table 2**
Bulk rock chemical composition of rock samples before treatment (treatment procedure is provided in Appendix A.). Analyses performed by Activation Labs (ActLabs), Ontario, Canada by ICP-OES for major elements and ICP-MS for trace elements.

| Sample[a] | SiO₂ % | TiO₂ % | Al₂O₃ % | Fe₂O₃ % | MnO % | MgO % | CaO % | Na₂O % | K₂O % | P₂O₅ % | LOI % | CO₂ % | Cl (ppm) | B (ppm) | Sm (ppm) | Gd (ppm) | U (ppm) | Th (ppm) | Cr (ppm) | Li (ppm) |
|---|---|---|---|---|---|---|---|---|---|---|---|---|---|---|---|---|---|---|---|---|
| KER 1903 | 48.30 | 2.74 | 15.24 | 11.62 | 0.16 | 5.72 | 7.83 | 3.02 | 2.80 | 0.47 | 1.41 | - | 62.84 | <10 | 6.8 | 5.5 | 1.6 | 7.8 | 140. | <15 |
| KER 1905 | 48.95 | 2.81 | 15.73 | 11.81 | 0.14 | 5.77 | 6.36 | 3.60 | 3.24 | 0.23 | 1.10 | - | 58.62 | <10 | 5.2 | 3.8 | 1.7 | 7.3 | 130 | 17 |
| KER 1906 | 48.53 | 2.60 | 16.33 | 11.01 | 0.12 | 5.72 | 6.08 | 3.53 | 2.99 | 0.19 | 1.40 | - | 64.69 | <10 | 4.4 | 3.1 | 1.5 | 7.3 | 130 | 16 |
| KER 1907 | 45.77 | 1.16 | 15.76 | 11.34 | 0.18 | 8.94 | 11.24 | 2.18 | 0.28 | 0.09 | 1.56 | - | 127.33 | <10 | 3.1 | 3.4 | < 0.1 | 0.3 | 360 | <15 |
| KER 1911 | 50.79 | 2.68 | 16.10 | 11.38 | 0.15 | 5.07 | 6.08 | 3.74 | 3.26 | 0.28 | 0.87 | - | 99.34 | <10 | 5.5 | 5.0 | 2.0 | 9.6 | 100 | <15 |
| KER 1912 | 53.10 | 2.00 | 17.76 | 8.79 | 0.11 | 3.80 | 6.59 | 4.21 | 2.90 | 0.36 | 0.60 | - | 51.24 | <10 | 4.2 | 3.7 | 1.6 | 5.7 | 80 | <15 |
| KER 1913 | 50.27 | 2.77 | 15.66 | 11.73 | 0.15 | 5.14 | 6.68 | 3.63 | 3.27 | 0.29 | 0.71 | - | 53.51 | <10 | 6.2 | 4.3 | 1.7 | 7.2 | 100 | <15 |
| KER 1928 | 61.74 | 0.21 | 18.51 | 5.01 | 0.11 | 0.06 | 0.13 | 6.13 | 5.95 | 0.07 | 1.29 | - | 4.21 | <10 | 6.3 | 5.9 | 5.5 | 32.8 | < 30 | <15 |
| KER 1929 | 59.25 | 0.99 | 15.90 | 7.01 | 0.13 | 2.35 | 2.46 | 4.81 | 3.59 | 0.17 | 3.71 | - | 31.83 | <10 | 12.1 | 11.1 | 8.1 | 37.7 | 90 | 25 |
| KER 1931 | 61.63 | 0.12 | 18.72 | 4.14 | 0.12 | 0.06 | 0.13 | 6.64 | 5.66 | 0.04 | 1.18 | - | 8.11 | <10 | 9.1 | 8.8 | 11.1 | 46.5 | < 30 | <15 |
| KER 1932 | 61.63 | 0.12 | 18.72 | 4.14 | 0.12 | 0.06 | 0.13 | 6.64 | 5.66 | 0.04 | 1.18 | - | 5.57 | <10 | 9.1 | 8.8 | 11.1 | 46.5 | < 30 | <15 |
| KER 1933 | 61.63 | 0.12 | 18.72 | 4.14 | 0.12 | 0.06 | 0.13 | 6.64 | 5.66 | 0.04 | 1.18 | - | 5.83 | <10 | 9.1 | 8.8 | 11.1 | 46.5 | < 30 | <15 |
| KER 1934 | 61.63 | 0.12 | 18.72 | 4.14 | 0.12 | 0.06 | 0.13 | 6.64 | 5.66 | 0.04 | 1.18 | - | 7.65 | <10 | 9.1 | 8.8 | 11.1 | 46.5 | < 30 | <15 |
| KER 1937 | 61.63 | 0.12 | 18.72 | 4.14 | 0.12 | 0.06 | 0.13 | 6.64 | 5.66 | 0.04 | 1.18 | - | 6.61 | <10 | 9.1 | 8.8 | 11.1 | 46.5 | < 30 | <15 |
| KER 1938 | 51.14 | 3.29 | 13.27 | 14.25 | 0.18 | 4.95 | 9.02 | 2.89 | 0.54 | 0.36 | 0.58 | - | 3.26 | <10 | 7.9 | 7.2 | 0.6 | 4.1 | 150 | <15 |
| KER 1939 | 51.14 | 3.29 | 13.27 | 14.25 | 0.18 | 4.95 | 9.02 | 2.89 | 0.54 | 0.36 | 0.58 | - | 5.75 | <10 | 7.9 | 7.2 | 0.6 | 4.1 | 150 | <15 |
| KER 1940 | 51.14 | 3.29 | 13.27 | 14.25 | 0.18 | 4.95 | 9.02 | 2.89 | 0.54 | 0.36 | 0.58 | - | 3.28 | <10 | 7.9 | 7.2 | 0.6 | 4.1 | 150 | <15 |

[a] Bulk rock composition was measured for KER 1931 and applied to KER 1932, 1933, 1934, and 1937 given their low Cl content and similar lithology. Bulk rock composition data was similarly applied to KER 1938, 1939, and 1940 from a same-lithology rock sample (KER, 1963; Tuestad, 2023) from the same region. Full explanation offered in Section 3.2.1.

less-than-ideal geometry of the boulder KER 1933 (8.5 ± 0.3 ka), we are inclined to believe that the older age of the KER 1932 more accurately reflects the age of moraine formation. This is further supported by the geomorphological mapping (Deline et al., 2024) and the Chi² test conducted on all six ages from both moraine ridges. Therefore, KER 1933; KER 1931 are considered outliers and are excluded from mean age calculations. The remaining four samples (KER, 1932; 1911, 1912, 1913) give a weighted mean age of 10.4 ± 1.2 ka for Mg-2 (Figs. 4 and 5).

### 5.3. ³⁶Cl ages from Mg-3 moraine boulders (n = 4)

Mg-3 is located about 2 km south of Mg-2, near the southern edge of Lake Guynemer (Fig. 3A and B). The central section of Mg-3 has been eroded by outwash flows from the glacier in the upper Guynemer basin, leaving Mg-3 latero-frontal moraine segments preserved on the northern and southern slope of the valley connecting the upper and lower Guynemer basins ((Fig. 3 A-B, Fig. 4). A total of four samples were taken from Mg-3, two from a moraine from the northern slope and two from the southern slope. From the northern slope, KER 1906 is from a 60 cm-high rounded boulder and KER 1907 is from a 1 m-high-sub angular boulder resting on the moraine surface, which give the ages 5.4 ± 0.3 ka and 1.7 ± 0.1 ka, respectively. From the southern slope, KER 1903; KER 1905 are sub-angular 30 cm- and 80 cm-high boulders (Fig. 2D) and yield the ages 1.2 ± 0.2 ka and 1.2 ± 0.2 ka, respectively. Based on the Chi² test, KER 1906 (5.4 ± 0.3 ka) is considered an outlier and is excluded from mean age calculations for Mg-3. Thus, the remaining three samples (KER 1907, 1903, 1905 give a weighted mean age of 1.4 ± 0.3 ka for Mg-3 (Figs. 4 and 5).

### 5.4. Erratic boulders

A total of five erratic boulders resting on bedrock were sampled in and around the Guynemer basin (Figs. 4, 5A and 6). Two erratic boulders, KER 1939; KER 1940, were sampled outside the Mg-1 extent on the N-NW slope of Mt. Louise, which yielded ages of 12.3 ± 0.2 ka and 13.5 ± 0.3 ka, respectively. Another erratic boulder, KER 1934, was sampled on Goeland Hill just north of the northern shore of Lake Guynemer between the Mg-2 and Mg-1 extents, which gives an age of 11.0 ± 0.4 ka. Finally, KER 1928 and KER 1929 were taken from two erratics on Col Louise, the bedrock threshold between the Guynemer basin and the lakes Louise to the S-SE, which yielded the ages 11.1 ± 0.3 ka and 10.4 ± 0.4 ka, respectively.

## 6. Discussion

### 6.1. Guynemer glacier fluctuation history

The presented ³⁶Cl exposure age dataset contributes to the existing chronology of the Late Glacial-Holocene glacier fluctuations on Kerguelen (Jomelli et al., 2017, 2018; Charton et al., 2020, 2022, 2024). The dataset suggests a general glacial retreat in the region that was punctuated by several glacial advances and/or stillstands throughout the Early and Late Holocene with no geomorphological indications for glacial activity in the Mid-Holocene (c. 8.2 ka – 4.3 ka; Walker et al., 2019).

The oldest ³⁶Cl ages in the dataset are from the two erratic boulder samples KER 1939; KER 1940 on Mt. Louise (216 and 238 m a.s.l., respectively), suggesting that the summit of Mt. Louise had become ice-free by 13.5 ± 0.3 ka and ice-thinning continued past 12.3 ± 0.2 ka (Fig. 6). These erratics are outside of the largest mapped Mg-1 extent of the Guynemer glacier, indicating that ice retreat from the Late Glacial to Early Holocene transition was punctuated by a glacial advance or still-stand around 11.5 ± 0.4 ka. During its largest Holocene extent, the Guynemer glacier was very likely conjoined with ice flowing into the Guynemer basin over Col Louise from the CIC outlet glaciers occupying

**Table 3**

$^{36}$Cl target element concentration measured on splits taken after chemical treatment as samples were being prepared for dissolution. Treatment procedure is provided in Appendix A. Analyses performed by Activation Labs (ActLabs) Ontario, Canada, by ICP-OES for major elements.

| Sample name | K$_2$O % | CaO % | TiO$_2$ % | Fe$_2$O$_3$ % |
|---|---|---|---|---|
| KER 1903 | 1.30 | 6.38 | 0.22 | 1.86 |
| KER 1905 | 0.86 | 5.54 | 0.09 | 1.50 |
| KER 1906 | 0.82 | 5.51 | 0.12 | 1.77 |
| KER 1907 | 0.22 | 9.68 | 1.47 | 11.85 |
| KER 1911 | 2.48 | 4.46 | 0.08 | 1.06 |
| KER 1912 | 1.91 | 5.41 | 0.08 | 0.83 |
| KER 1913 | 1.95 | 4.85 | 0.09 | 0.98 |
| KER 1928 | 7.05 | 0.13 | 0.04 | 1.22 |
| KER 1929 | 5.03 | 0.13 | 0.08 | 2.06 |
| KER 1931 | 7.60 | 0.11 | 0.03 | 1.27 |
| KER 1932 | 7.64 | 0.13 | 0.05 | 1.21 |
| KER 1933 | 7.36 | 0.18 | 0.05 | 1.22 |
| KER 1934 | 8.11 | 0.41 | 0.03 | 0.93 |
| KER 1937 | 7.52 | 0.15 | 0.06 | 1.17 |
| KER 1938 | 0.28 | 9.22 | 1.38 | 12.54 |
| KER 1939 | 4.16 | 1.06 | 2.07 | 2.80 |
| KER 1940 | 0.95 | 1.67 | 2.17 | 7.33 |

the Lake Louise region (Fig. 3C). As deglaciation progressed from the Late Glacial into the Holocene, $^{36}$Cl ages from erratic boulders KER 1928 and KER 1929 on Col Louise (151 and 159 m a.s.l.) suggest that the threshold between the Guynemer glacier and the CIC outlets became ice free around 11.1 ± 0.3 ka to 10.4 ± 0.4 ka. Given the spread between these two ages, the exact timing of the separation of the Guynemer glacier from the CIC outlet glaciers is unclear. The Mg-1 extent was followed by ice retreat, and the erratic boulder KER 1934 indicated that the Goeland hill (117 m a.s.l.) near the northern shore of Lake Guynemer was ice free by 11.0 ± 0.4 ka, which also overlaps with the deglaciation of Col Louise (Fig. 6). Ice retreat was subsequently interrupted by a glacial advance or stillstand at 10.4 ± 1.2 ka when the glacier front was positioned at its Mg-2 extent, depositing the moraine on the northern shore of Lake Guynemer (Figs. 4 and 6). Thus, the Guynemer glacier was likely separated from the CIC outlets by the time of its Mg-2 extent.

Following Mg-2, the glacier retreated significantly during the Mid-Holocene. While the exact extent of the retreat is unknown, the absence of moraines between Mg-2 and Mg-3 suggests that the glacier retreated at least to the mouth of the upper Guynemer basin before the Late Holocene re-advance around 1.4 ± 0.3 ka marked by Mg-3. Indeed, Mid-Holocene moraines could potentially have been deposited within the Mg-3 limits but would have been erased by the subsequent Mg-3 advance. Over the course of the last millennium, the Guynemer glacier underwent an overall retreat that was punctuated by three undated moraine-building stages Mg-4, 5 and 6 (Fig. 6). By 1963, the glacier front had retreated a net distance of c. 600 m since its Mg-3 position, at which point it only occupied the upper Guynemer basin (Figs. 4 and 6). In the following decades, the glacier underwent accelerated retreat towards its 2019 position, retreating another 1.5 km in only half a century and allowing Lake Surprise to form in the glacial over-deepening in the upper Guynemer basin (Figs. 4 and 6; Deline et al., 2024).

### 6.2. Comparison with existing Kerguelen glacial chronology

The existing glacial chronology of Kerguelen ranges from MIS 3 to the last few centuries based on $^{36}$Cl ages from erratic boulders, glacially polished bedrock, and moraine boulders from CIC glaciers as well as local glaciers around the archipelago (Jomelli et al., 2017, 2018; Charton et al., 2020, 2022). Our $^{36}$Cl chronology of the Guynemer glacier fluctuations generally corroborates the overall deglaciation trend since the Late Glacial demonstrated by previous studies, albeit with some minor differences. The existing $^{36}$Cl chronology suggests progressive deglaciation during the Late Glacial, which was interrupted by a glacial advance likely during the ACR (Fig. 7F; Jomelli et al., 2017,

2018; Charton et al., 2022).

Multi-proxy-based climate reconstructions from peat sequences from the eastern part of Kerguelen indicate that wetter and windy conditions started to emerge around 13.6 ka, which lasted until a transition into warmer and dryer conditions around 11.6 ka (van der Putten et al., 2015). While numerous Late Glacial moraines are found on Kerguelen (see Section 2.2; Fig. 6F), no evidence of a Late Glacial advance has been found at Guynemer at this time. Nevertheless, given that there is widespread evidence of Late Glacial ice advances on Kerguelen, it is possible that a Late Glacial advance did occur at Guynemer, but extended offshore into the fjord Baie du Repos as suggested by the glacial overdeepening of c. 175 m a.s.l., 5.5 km downstream from the Mg-1 front. Still, the 13.5 ka deglaciation age of Mt. Louise, taken at face value, indicates that ice was thinning in the Guynemer basin in the middle of the ACR period. Therefore, if there was a Late Glacial advance in the area, it would most likely have occurred before 13.5 ka, leaving no moraine or erratics on Mt. Louise as it was still covered by ice.

No evidence of Early Holocene moraines like 11.5 ka Mg-1 or 10.4 ka Mg-2 has previously been identified elsewhere on Kerguelen. Moreover, both Mg-1 and Mg-2 were deposited during a transition into warmer and dryer conditions as suggested by climate reconstructions from peat sequences from the Courbet peninsula (van der Putten et al., 2015). Nevertheless, given the present-day dichotomy in precipitation between eastern and western Kerguelen, the Courbet peninsula to the east could have experienced drier conditions whereas the CIC region to the west continued to be wet enough for glacial advances in the Early Holocene. Moreover, the presence of the large ice cap would likely have impacted local wind and patterns on the western sector of the archipelago (e.g., Parish and Cassano, 2003; van As et al., 2014) and such patterns would shift as ice cap topography changed over time. Early Holocene pauses in glacial retreat at Guynemer may also be explained by local glacier dynamics. Indeed, the glacial overdeepening occupied by Lake Guynemer is quite deep, with Lake Guynemer having a water depth of up to 90 m and an additional +20 m of lacustrine sediment deposits (Deline et al., 2024). The Guynemer glacier ice dynamics would have shifted to that of a local glacier following its separation from larger ice bodies to the south between c. 10–11 ka. Numerous studies have demonstrated the higher sensitivity of mountain glaciers to climatic signals than that of larger ice bodies (e.g., Bach et al., 2018). As a smaller local glacier, the Guynemer glacier was probably more sensitive to changes in climate than CIC outlet glaciers, which may also help explain the presence of Early Holocene moraines at Guynemer that have not presently been found elsewhere on Kerguelen.

Guynemer glacial chronology after the Early Holocene agrees well with the previously existing Kerguelen glacial chronology showing an absence of geomorphologic evidence of glacial activity during the Mid-Holocene, which suggests that glaciers were significantly smaller in the Mid-Holocene than in the Late Holocene when glaciers underwent a re-advance (Frenot et al., 1997; Jomelli et al., 2017; Charton et al., 2020, 2022). Radiocarbon ages from sediment cores taken just offshore from the Ampère delta, suggest very high rates of glaciomarine sedimentation into the fjord during the Late Holocene, with an increase in sedimentation rate occurring around 1110–1290 CE (Jomelli et al., 2017). The increase in sedimentation rate corresponds to the deposition of the M1 Ampère moraine (1.00 ± 0.47 ka; Figs. 1A and 7F; Charton et al., 2022), demonstrating a resurgence in glacial activity around 1–1.5 ka. The Mg-3 moraine at Guynemer, dated to 1.4 ± 0.3 ka, provides further corroborating evidence of a Late Holocene re-advance, as it formed concurrently with the M1 Ampère moraine as well as the A2a Arago glacier moraine dated to 1.12 ± 0.33 ka (Figs. 1A and 7F; Charton et al., 2022).

At Guynemer, three mapped moraine sets upstream from Mg-3 (Mg-4,5 and 6) remain undated. Younger than Mg-3, these moraines were formed within the last millennium and pre-date the 1963 extent. A similar pattern of moraine deposition is observed at Ampère, where a younger M2 moraine has been dated to 480 ± 290 a with several

**Table 4**

$^{36}$Cl isotope data and exposure dating results. Cl ratios were measured at the Scottish Universities Environmental research Centre (SUERC) AMS Laboratory. $^{36}$Cl concentration was calculated using isotope dilution using methods described in Section 3.2.1. Ages presented were calculated using LSDn scaling (Lifton et al., 2014).

| Sample name | Sample weight (g) | mass of Cl in spike (mg) | $^{36}$Cl/$^{35}$Cl ($10^{-14}$)[a] | $^{36}$Cl/$^{37}$Cl ($10^{-14}$) | $^{37}$Cl/$^{35}$Cl ($10^{-1}$) | [Cl] in sample (ppm) | [$^{36}$Cl] $10^3$ atoms g$^{-1}$ | Age (a)[b] |
|---|---|---|---|---|---|---|---|---|
| KER 1903 | 23.946 | 1.053 | 1.17 ± 0.05 | 1.79 ± 0.07 | 1.86 | 63.73 | 18 ± 1.1 | 1180 ± 200 (190) |
| KER 1905 | 26.239 | 1.036 | 1.16 ± 0.06 | 1.76 ± 0.09 | 1.89 | 59.44 | 16.4 ± 1.2 | 1160 ± 220 (190) |
| KER 1906 | 25.506 | 0.999 | 2.63 ± 0.08 | 3.86 ± 0.12 | 1.95 | 65.55 | 45.6 ± 1.7 | 5400 ± 420 (270) |
| KER 1907 | 43.667 | 1.037 | 0.77 ± 0.04 | 0.89 ± 0.05 | 2.46 | 128.59 | 17.7 ± 1.5 | 1700 ± 350 (140) |
| KER 1911 | 45.229 | 1.076 | 6.14 ± 0.17 | 7.35 ± 0.21 | 2.38 ± 0.02 | 100.36 | 131.3 ± 7.7 | 10,800 ± 1550 (890) |
| KER 1912 | 46.334 | 1.111 | 6.37 ± 0.19 | 8.74 ± 0.26 | 2.05 ± 0.02 | 51.87 | 84.8 ± 4.5 | 9700 ± 1000 (640) |
| KER 1913 | 26.100 | 1.047 | 5.26 ± 0.16 | 8.21 ± 0.24 | 1.82 ± 0.01 | 54.29 | 87.3 ± 3.2 | 10,600 ± 1010 (470) |
| KER 1928 | 46.577 | 1.099 | 24.01 ± 0.69 | 81.3 ± 2.34 | 0.83 | 4.44 | 135.4 ± 4 | 11,200 ± 840 (310) |
| KER 1929 | 27.733 | 1.044 | 10.01 ± 0.29 | 18.3 ± 0.54 | 1.56 | 32.41 | 129 ± 4 | 10,400 ± 880 (430) |
| KER 1931 | 39.574 | 0.980 | 19.48 ± 0.51 | 52.15 ± 1.37 | 1.06 | 8.38 | 126.1 ± 3.4 | 9200 ± 730 (290) |
| KER 1932 | 46.914 | 1.101 | 23.29 ± 0.67 | 70.91 ± 2.05 | 0.92 | 5.82 | 135.7 ± 4.1 | 10,400 ± 840 (330) |
| KER 1933 | 46.577 | 1.104 | 18.25 ± 0.53 | 54.83 ± 1.58 | 0.93 | 6.08 | 107.5 ± 3.2 | 8300 ± 660 (260) |
| KER 1934 | 39.540 | 1.033 | 23.73 ± 0.74 | 66.44 ± 2.08 | 1.02 | 7.94 | 159.5 ± 5.1 | 11,000 ± 940 (380) |
| KER 1937 | 41.718 | 1.096 | 23.87 ± 0.69 | 71.07 ± 2.05 | 0.94 | 6.89 | 157.3 ± 4.7 | 11,100 ± 870 (330) |
| KER 1938 | 41.940 | 0.856 | 13.99 ± 0.33 | 49.15 ± 1.18 | 0.81 | 3.46 | 65.7 ± 1.7 | 11,800 ± 820 (300) |
| KER 1939 | 41.478 | 1.078 | 15.91 ± 0.3 | 49.72 ± 0.93 | 0.91 | 6.02 | 100.6 ± 2 | 12,300 ± 860 (250) |
| KER 1940 | 40.169 | 0.998 | 7.22 ± 0.17 | 27.03 ± 0.63 | 0.76 | 3.51 | 39.3 ± 1.1 | 13,500 ± 770 (340) |

| Blanks[c] | | mass of Cl in spike (mg) | $^{36}$Cl/$^{35}$Cl ($10^{-15}$) | $^{36}$Cl/$^{37}$Cl ($10^{-14}$) | $^{37}$Cl/$^{35}$Cl ($10^{-1}$) | Cl$_{blank}$ ($10^{19}$ atoms) | $^{36}$Cl$_{blank}$ ($10^5$ atoms) | |
|---|---|---|---|---|---|---|---|---|
| BS 21-1 | - | 2.039 | 4.24 ± 0.37 | 2.53 ± 0.22 | 0.48 | 1.934 ± 0.005 | 1.03 ± 0.09 | - |
| BS 21-2 | - | 1.54 | 6.84 ± 0.79 | 3.97 ± 0.46 | 0.49 | 1.461 ± 0.004 | 1.25 ± 0.14 | - |
| BS 21-3 | - | 1.895 | 2.26 ± 0.6 | 1.37 ± 0.36 | 0.47 | 1.797 ± 0.004 | 0.51 ± 0.14 | - |
| BS 21-4 | - | 1.69 | 15.5 ± 3.51 | 8.75 ± 1.16 | 0.51 ± 0.01 | 1.603 ± 0.012 | 3.1 ± 0.7 | - |
| BS 21-5 | - | 1.974 | 4.68 ± 2.53 | 2.86 ± 0.46 | 0.46 | 1.872 ± 0.004 | 1.1 ± 0.59 | - |
| BS 21-6 | - | 1.983 | 4.87 ± 0.81 | 2.95 ± 0.49 | 0.46 | 1.881 ± 0.004 | 1.15 ± 0.19 | - |
| BS 21-7 | - | 1.976 | 5.3 ± 1.4 | 3.12 ± 0.72 | 0.48 | 1.874 ± 0.004 | 1.24 ± 0.33 | - |

[a] Ratios are normalized to the $^{36}$Cl standard Z93-0005 produced at Purdue University's Prime Lab with a $^{36}$Cl/$^{35}$Cl ratio of 1.2 x $10^{-12}$ and a $^{37}$Cl/$^{35}$Cl ratio of 1.3 x $10^{-3}$ measured at the SUERC AMS Laboratory.

[b] Ages presented with total uncertainties (1σ) with analytical (internal) uncertainties in parentheses.

[c] BS 21–3 was used for blank subtraction. The $^{36}$Cl/Cl ratio of 2.84 ± 1.87 x $10^{-15}$ was subtracted in isotope dilution calculations described in Appendix B. The standard deviation of all blanks' (excluding BS 21–4) $^{36}$Cl/Cl ratio was applied as its uncertainty. BS 21–4 was excluded because its $^{36}$Cl concentration is more than double that of the other blanks included in this study.
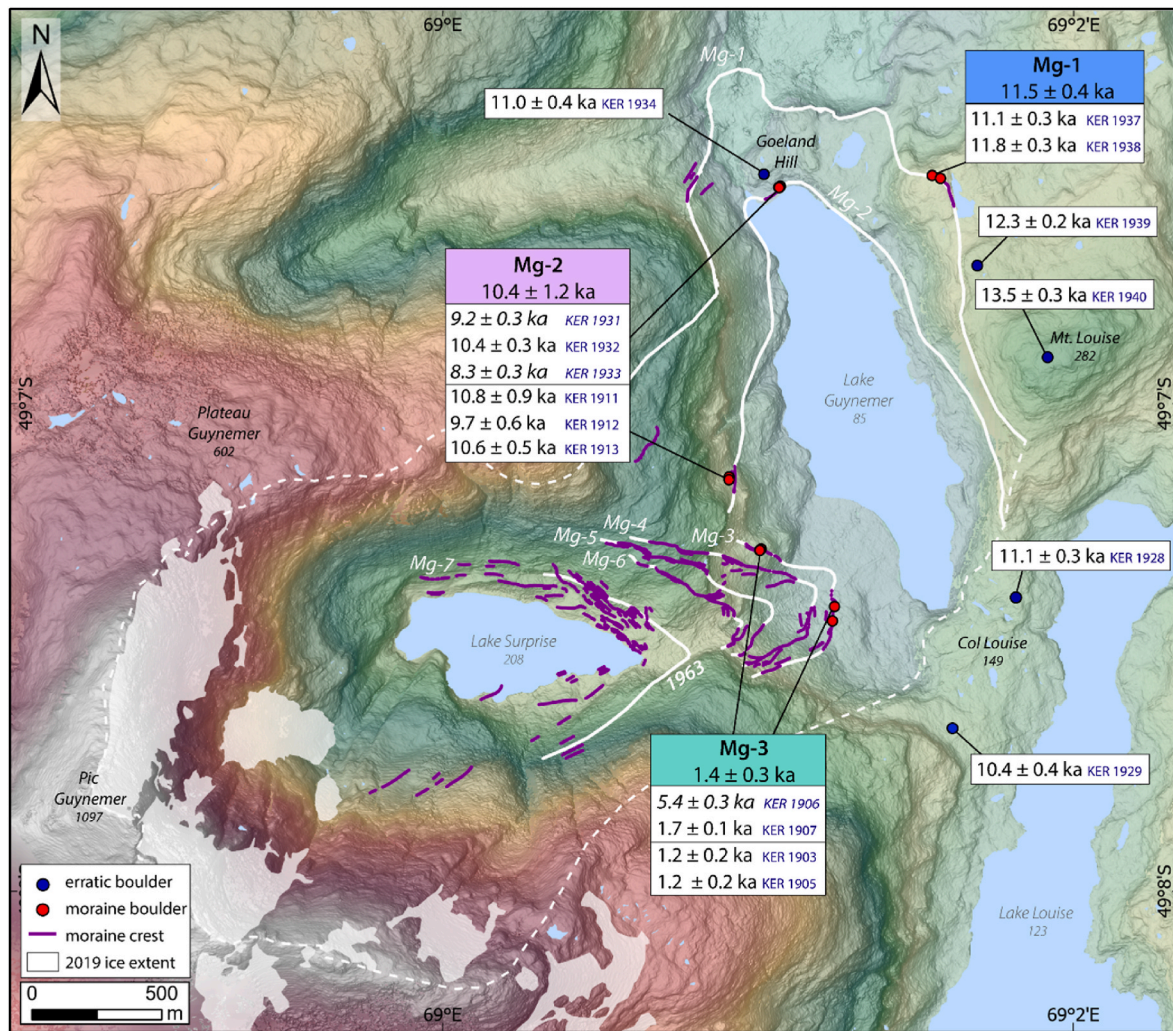
**Fig. 4.** DEM-based map of the Guynemer study area showing $^{36}$Cl dating results (DEM derived from Pléiades orthoimages). Dating results are also shown in Table 4. Age uncertainties are analytical uncertainty only. Ages in italics are designated as outliers and are not included in mean age calculations. Dashed white line: ice divide, solid white line: reconstructed paleo ice margins Mg-1 to Mg-7 after Deline et al. (2024).

undated moraines further upstream that pre-date the 1970s (Fig. 7F; Frenot et al., 1993; Verfaillie et al., 2021; Charton et al., 2022). The deposition of the M2 moraine corresponds with the so-called Little Ice Age cold event (LIA, *c.* 1400–1870 Solomina et al., 2015; Solomina et al., 2015), which has been widely recorded by glacial re-advances in the Northern Hemisphere (*e.g.* Ivy-Ochs et al., 2009; Solomina et al., 2015; Rowan, 2017; Nicolussi et al., 2022), but less so in the Southern Hemisphere (*e.g.* Neukom et al., 2014; Chambers et al., 2014). Considering the similar pattern of moraine deposition between the Guynemer and Ampère glaciers, we can reasonably project that the undated moraines at Guynemer also were formed during the LIA.

### 6.3. Comparison with other sub-Antarctic glacial chronologies and climatic proxies

The updated Kerguelen glacier chronology is generally consistent with glacier records from other sub-Antarctic regions, albeit with some differences. Newly documented Early Holocene moraines suggest that some glaciers on Kerguelen like the Guynemer glacier may have been at their post-ACR maxima in the Early Holocene as opposed to during Late Holocene re-advances as previously suggested by Charton et al. (2022). Some glacier chronologies from Patagonia demonstrate that following glacier expansion during the ACR, glaciers generally retreated significantly during the Early Holocene (Strelin et al., 2011, 2014; Kaplan

et al., 2016; Reynhout et al., 2019). Patagonian glacier sites north of 50°S show an absence of Early Holocene moraines but demonstrate evidence of numerous Mid-Holocene advances when glaciers reached their largest Holocene extents between c. 6 ka and 4.5 ka (Strelin et al., 2014; Kaplan et al., 2016). On the other hand, Early Holocene moraines have been identified between 49 and 50°S in the southern Patagonia Icefield, indicating that glaciers reached their post-ACR maxima between c. 9 ka and 11.6 ka (Reynhout et al., 2019). Subsequent glacier advances occurred throughout the Mid- to Late Holocene that were progressively smaller in magnitude (Kaplan et al., 2016; Reynhout et al., 2019).

Comparatively, glaciers in New Zealand also underwent ice retreat following an ACR expansion. New Zealand glaciers reach their maximum post-ACR extents in the Early Holocene followed by a net retreat interrupted by numerous re-advances in the Mid- and Late Holocene (Schaefer et al., 2009; Putnam et al., 2010; Kaplan et al., 2013). In the south Atlantic Ocean, glaciers on South Georgia similarly experienced several Early Holocene advances at *c.* 10.5 ka and 9 ka, followed by progressive retreat punctuated by periods of glacial expansion in the Mid to Late Holocene (van der Bilt et al., 2017; Oppedal et al., 2018; Bakke et al., 2021).

The most noticeable difference in glacier records on Kerguelen compared to other still-glaciated sub-Antarctic regions is the lack of any geomorphological evidence of Mid-Holocene glacier activity on
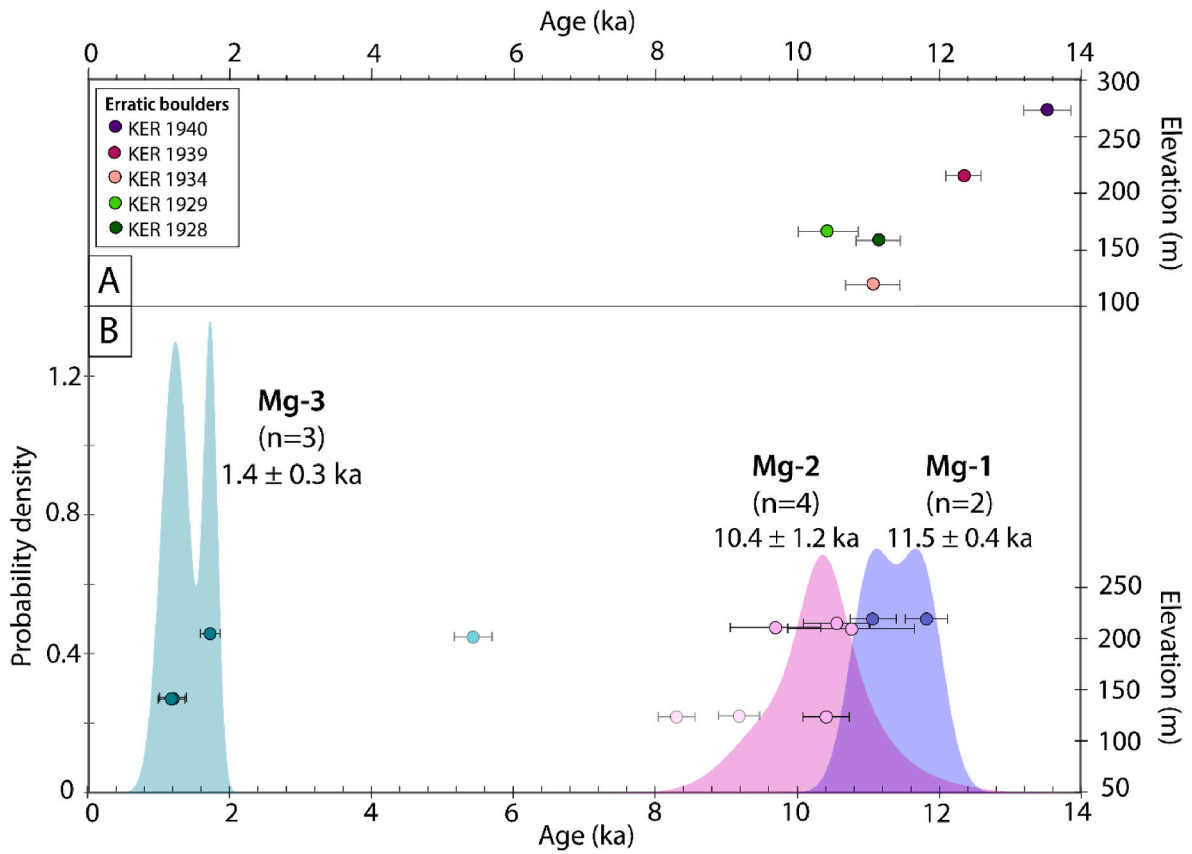
**Fig. 5. (A)** Age *vs.* elevation plot of erratic boulder samples showing a general trend of decreasing age with lower elevations. **(B)** Probability density plots of dated moraines showing the sum frequency curve for each landform. Individual dated samples are plotted against elevation (lower right axis) with corresponding colors to the probability density curves of each moraine. Outliers are denoted by translucent data points and are not included in weighted mean age calculations of each moraine.
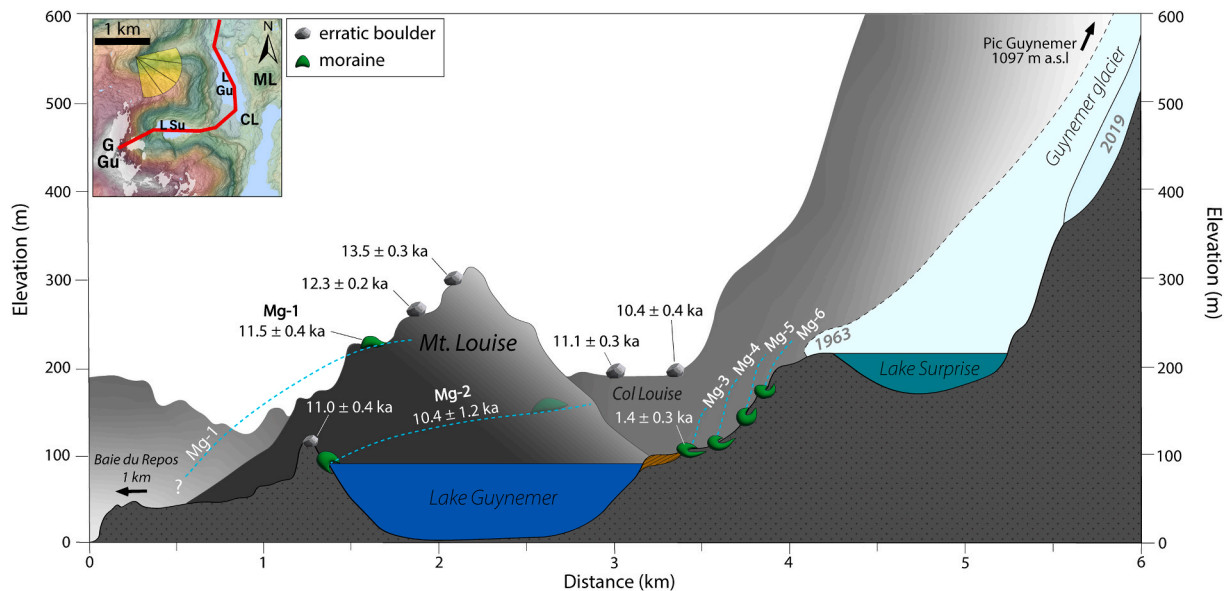


**Fig. 6.** Schematic transect of the upper and lower Guynemer basins with $^{36}$Cl ages from this study plotted at their respective sample sites along the transect. Paleoglacier front positions (blue dotted lines) are estimated based on corresponding moraine locations/elevations. The inset at the top left shows the path of the transect (red line) and viewing perspective (yellow fan). GGu: Guynemer glacier, LSu: Lake Surprise, LGu: Lake Guynemer, CL: Col Louise, ML: Mt Louise. The transect starts from the 2019 position of the Guynemer glacier on the right, moving through the Lake Surprise and turning northwards through Lake Guynemer and continuing northwards towards the fjord Baie du Repos. Mg-2 lateral moraine is located on the slope opposite the valley from Mt. Louise, but it is depicted at the corresponding elevations on Mt. Louise on the figure for interpretive purposes. Lake colors reflect the true color of the lakes, as Lake Surprise is a lighter blue-green color due to direct inflow from the Guynemer glacier. Topographic profiles are shown with a 5.3 × vertical exaggeration.
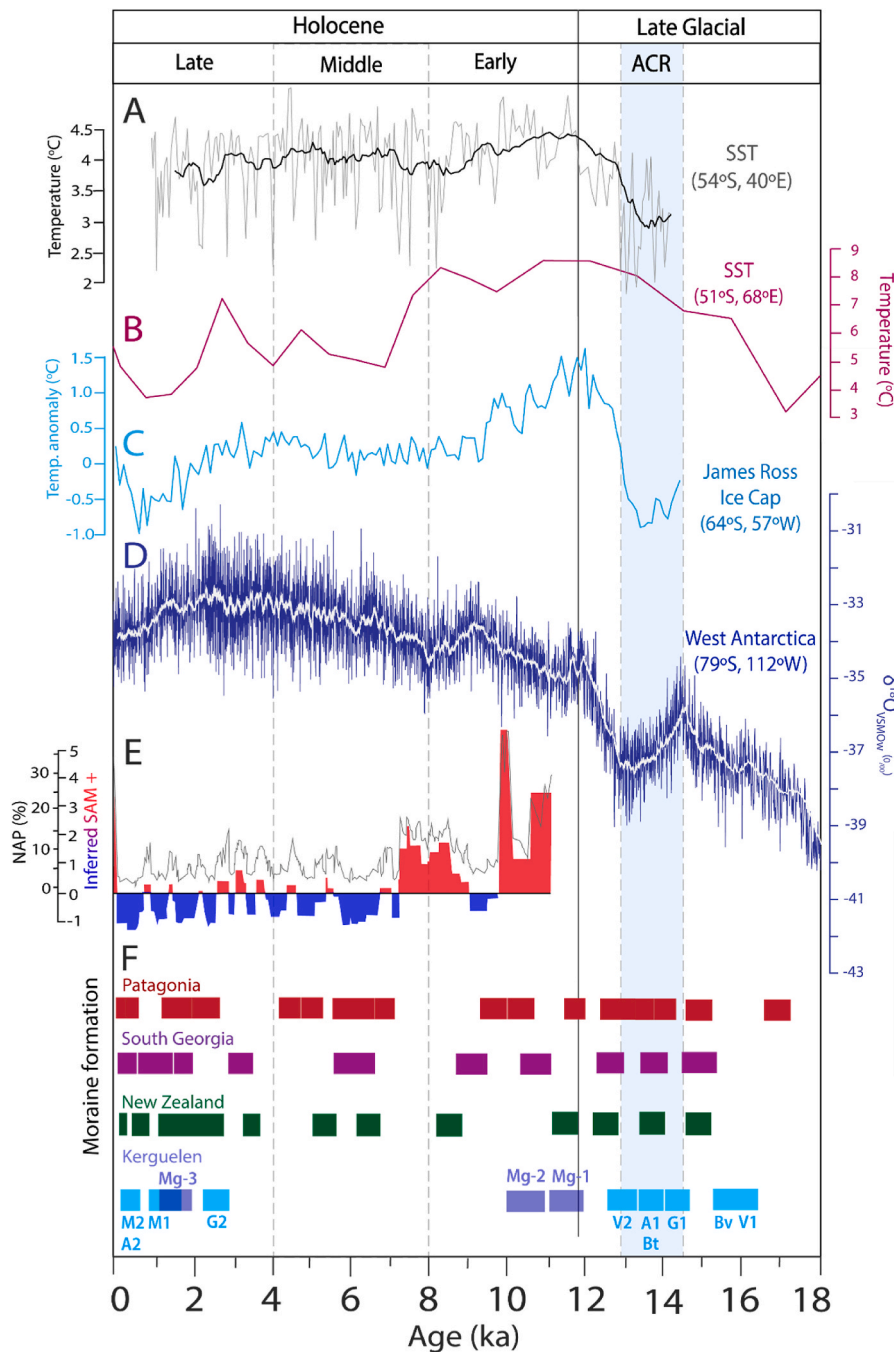
**Fig. 7.** (A) Mean summer sea surface temperature reconstruction based on diatoms from marine core COR1GC in the southwestern Indian Ocean (Orme et al., 2020). **(B)** Sea surface temperature reconstruction based on diatom assemblages from marine core MD11-3353 in the southern Indian Ocean (Civel-Mazens et al., 2021). **(C)** Summer temperature reconstruction based on deuterium variations in an ice core from the James Ross Ice Cap (Mulvaney et al., 2012). **(D)** $\delta^{18}O$ ratio from the West Antarctic Ice Sheet Divide (WAIS Divide Project Members, 2013). **(E)** SAM-like index (red: positive, blue: negative) reconstructed from Lago Cipreses (51°S) non-arboreal pollen (NAP; black curve) from Patagonia (Moreno et al., 2018). **(F)** Periods of moraine formation in Patagonia (Murray et al., 2012; Kaplan et al., 2016; Reynhout et al., 2019, Mendelová et al., 2020), South Georgia (Bakke et al., 2021), New Zealand (Schaefer et al., 2009; Putnam et al., 2010; Kaplan et al., 2013), and Kerguelen (purple: this study; light blue: Jomelli et al., 2017, 2018; Verfaillie et al., 2021; Charton et al., 2020, 2022). Moraine names (M2, A2, etc.) are as they as presented in their respective papers, except for the Bontemps moraine abbreviated as 'Bt' and Belvedere moraine is abbreviated as 'Bv'.

Kerguelen (Fig. 7F), indicating that Mid-Holocene glacier extents were rather small and within the limits of the Late Holocene expansion. This pattern of glacial evolution differs from New Zealand, South Georgia and most of Patagonia previously discussed, which experienced a net decrease in glacial extents throughout the Holocene with the smallest extents in the Late Holocene.

Atmospheric temperature changes derived from the West Antarctic Ice Sheet Divide ice core records show a dramatic increase in $\delta^{18}O$ values

following the ACR cold period until around 12 ka, after which there is a gradually increasing trend until the Late Holocene when values decreased again, particularly during the last millennium or so (Fig. 7D; WAIS Divide Project Members, 2013). Similarly, summer temperature reconstructions from the James Ross Ice Cap (Mulvaney et al., 2012) also show abrupt warming after the ACR until c. 11 ka when temperatures dropped and remained relatively stable through the Mid-Holocene until around 4 ka when temperatures dropped again entering the Late

Holocene (Fig. 7C). Deglaciation occurring at Guynemer from 13.6 ka and past 12.4 ka corresponds with the abrupt warming shown in both the West Antarctic and at James Ross (Fig. 7C and D). Local sea surface temperature (SST) reconstructions from the MD11-3353 core located just southwest of Kerguelen in the southern Indian Ocean (Civel-Mazens et al., 2021) show a net warming trend during the ACR until about 12 ka, albeit with low resolution, which corresponds to Guynemer ice-thinning on Kerguelen *c.* 13.6–12.4 ka (Fig. 7B). A similar trend is also observed in another core COR1GC from the southwestern Indian Ocean, from which mean summer SST reconstructions show a steep onset of warming in the mid-ACR just after 14 ka (Orme et al., 2020, Fig. 7A). Glacial advances and/or standstills at Mg-1 and Mg-2 also coincide with warm, but cooling SSTs at the onset of the Holocene (Fig. 7A, B), a cooling trend that is recorded at the James Ross Ice cap as well (Fig. 7C). Nonetheless, the net decrease in ice extent from Mg-1 to Mg-2 is consistent with the overall warming trend shown by regional SST reconstructions (Fig. 7A and B). Glacial fluctuations on Kerguelen are believed to be driven by a combination of SST and SAM-driven precipitation variations associated with the position of the SHW belt (van der Putten et al., 2015; Charton et al., 2022). The only precipitation-based SAM reconstruction that reaches far back enough in time to the Early Holocene is based on a Patagonian Lago Cipreses non-arboreal pollen record (Fig. 7E; Moreno et al., 2018). This reconstruction indicates that SAM + like conditions during the Early Holocene would have resulted in relatively dry conditions at Kerguelen (Fig. 7E). Dry conditions combined with relatively higher SST is believed to be the driving factor for the smaller extent of Kerguelen glacier from the Early into the Mid-Holocene (Charton et al., 2022). Nonetheless, Early Holocene moraine Mg-1 and Mg-2 reveal that some glaciers on the archipelago remained at relatively larger extents well into the Early Holocene despite predominantly warm and dry conditions. A transition into frequent SAM - like states in the Late Holocene would result in increased precipitation coinciding with decreasing temperature (Fig. 7A–E), resulting in glacial expansions recorded on Kerguelen, as well as most other southern mid-latitude glacial chronologies (Fig. 7F).

## 7. Conclusion

This study aimed to provide chronological constraints on paleo-glacier reconstructions from a local cirque glacier Guynemer north of the Cook Ice Cap on the Kerguelen archipelago using $^{36}$Cl exposure dating of moraine and erratic boulders. Deglaciation at Mt. Louise commenced around 13.5 ka and continued past 12.4 ka, during which time the ice occupying the Guynemer basin likely was still connected to the CIC outlet glaciers. The two outermost moraines were formed at c. 11.5 ka and 10.4 ka, providing the first evidence of ice advances/still-stands during the Early Holocene on Kerguelen. Erratic boulders on Col Louise indicate that the Guynemer glacier separated from ice flowing from the Lake Louise region between 10 and 11 ka. Similar to previous studies on Kerguelen, no moraines from the Mid-Holocene have been found at Guynemer, confirming that the glaciers of the archipelago had a limited extent throughout most of the Holocene following Early Holocene advances/standstills. A Late Holocene advance that occurred at *c.* 1.4 ka corroborates Late Holocene glacial expansion documented at several sites on the archipelago. While the 1.4 ka advance was significantly smaller than the glacial extent during the Early Holocene, the lack of moraines from between 10.4 ka and 1.4 ka suggests the more expansive Late Holocene advance likely erased any potential moraines deposited by Mid-Holocene glacier activity.

Early Holocene moraines are a new contribution to the existing $^{36}$Cl

glacial chronology on Kerguelen. Although unique to the Guynemer region thus far, these moraines suggest that the glacier extent was still relatively large following the Holocene transition compared to the subsequent Late Holocene re-advances. Comparisons with other sub-Antarctic glacial chronologies show that Kerguelen experienced a different pattern of glacier fluctuations since the Late Glacial. While most of Patagonia, New Zealand and South Georgia underwent decreasing glacial extent through the Holocene, glaciers on Kerguelen had larger extents in last couple of millennia than they did in at least the last 10 ka.

## Declaration of competing interest

The authors declare that they have no known competing financial interests or personal relationships that could have appeared to influence the work reported in this paper.

## Data availability

Data will be made available on request.

## Appendix

### Appendix A. *Laboratory procedure for preparation of $^{36}$Cl targets*

For the thirteen samples processed as feldspar concentrate samples, the feldspar content of each sample was concentrated by removing magnetic minerals through mineral separation using a Franz magnetic separator. Of the 13 samples, 9 were etched in a mixture of diluted HF/HNO$_3$ to remove mineral inclusions (Schimmelpfennig et al., 2009), which removed 5–10% of the samples. The remaining four samples (KER, 1903; 1905, 1906, 1929) were only leached in 3% HNO$_3$ due to limited sample mass. Four whole-rock samples (Table 1) were etched with a diluted HF/HNO$_3$ mixture for 48–72 h during which around 25–40% of each sample was removed to eliminate any potential Cl-rich inclusions as well as meteoric $^{36}$Cl (Schimmelpfennig et al., 2009). This etching process was implemented following previous studies with $^{36}$Cl dating on Kerguelen (Jomelli et al., 2017, 2018; Verfaillie et al., 2021; Charton et al., 2020, 2022, 2024) which produced consistent results by removing up to 40% of their whole rock samples through etching. At this stage, 5–10 g aliquots of all the treated samples were taken and sent for major element analysis by ICP-OES at Actlabs to measure target mineral composition (Table 3).

Approximately 25–55 g of each sample was weighed and spiked with 2 mg of isotopically enriched chloride carrier (99.63 % enrichment, ICON). Samples were then dissolved in a mixture of HF/HNO$_3$ and placed on a shaker table for several days, followed by an ultrasonic bath and monitored until full dissolution. An additional 5–10 ml of HF was added to select slower-dissolving samples to encourage dissolution. Once dissolved, fluorides and any undissolved material were centrifuged out and removed. AgNO$_3$ was added to precipitate AgCl out of the sample solution, which was then cleaned by being dissolved and reprecipitated using NH$_4$OH and HNO$_3$, respectively. Since sulfur-36 ($^{36}$S) can interfere with the measurement of $^{36}$Cl, BaNO$_3$ was added to precipitate BaSO$_4$. Samples were left up to 4–7 days in the dark and then filtered with unbleached syringe filters. Finally, AgNO$_3$ was added again and HNO$_3$ was used to precipitate AgCl, which was rinsed, dried and pressed into copper cathodes.

### Appendix B. *Blank subtraction*

The seventeen samples included in this paper were processed as part of a larger assemblage of samples collected from the study area and surrounding region during the 2019 field campaign. In total, this assemblage was processed together with 7 process blanks outlined in Table 4, with one blank included per batch and two blanks per double-batch. Blanks were prepared with comparable amounts of carrier and HF/HNO$_3$ as other samples and then were processed alongside the unknowns throughout the entire procedure described above. The unknown samples were blank corrected with the lowest concentration blank (BS 21–3) and the standard deviation of all blanks' $^{36}$Cl concentration was applied as its uncertainty. The lowest blank was used for all samples because it was the only blank that did not yield negative $^{36}$Cl concentrations for the youngest samples in the sample assemblage.

### Appendix C. *$^{36}$Cl production rates used in this study vs. previous studies*

Multiple $^{36}$Cl production rates were used in this study, specifically for the spallation of Ca, the spallation of K, and the production rate of epithermal neutrons from fast neutrons in the atmosphere at the rock surface (Table C1). The degree to which the different production rates affect the resulting ages varies with the chemical composition of each sample which dictates the percentage of $^{36}$Cl production coming from each production pathway. A ternary diagram displaying the percentage of total $^{36}$Cl production from Ca, K and Cl is included in Fig. C1.

**Table C1**
Published $^{36}$Cl production rates (sea level and high latitude) used to calculate $^{36}$Cl exposure ages in this study compared with previous studies on Kerguelen. Production rates used in this study are those employed by the CRONUScalc $^{36}$Cl exposure age calculator. Rates are presented with 1σ uncertainties.

|  |  | LSDn scaling | St scaling | Reference |
|---|---|---|---|---|
| **This study** | Spallation of Ca[a] | 55.6 ± 4.2 | 52.5 ± 3.6 | Marrero et al., 2021 |
|  | Spallation of K[b] | 156 ± 12 | 151 ± 10 | Marrero et al., 2021 |
|  | Pf(0)[c] | 714 ± 191 | 649 ± 201 | Marrero et al., 2021 |
| **Previous studies*** | Spallation of Ca[a] |  | 42.2 ± 4.8 | Schimmelpfennig et al., 2011 |
|  | Spallation of K[b] |  | 148.1 ± 7.8 | Schimmelpfennig et al., 2014 |
|  | Pf(0)[c] |  | 626 | Phillips et al., 2001 |
|  |  |  | 649** | Marrero et al., 2021 |

Production rate of $^{36}$Cl by spallation of Ca in atoms $^{36}$Cl (g Ca)$^{-1}$ yr$^{-1}$.
Production rate of $^{36}$Cl by spallation of K in atoms $^{36}$Cl (g K)$^{-1}$ yr$^{-1}$.
Production rate of epithermal neutrons from fast neutrons in the atmosphere at the rock surface/atmosphere interface in neutrons (g air) yr$^{-1}$.
*Jomelli et al. (2017, 2018), Charton et al., 2020, 2022, Verfaillie et al. (2021).
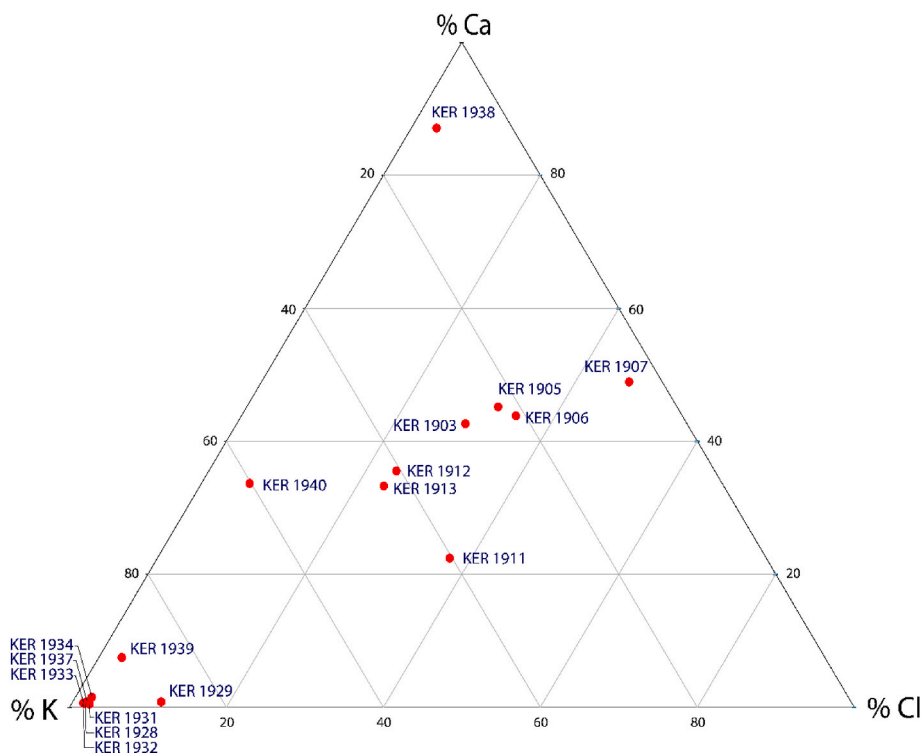**Pf(0) used by Charton et al. (2022)

**Fig. C1.** Ternary diagram of percentage of total $^{36}$Cl production from each production pathway (Ca, K and Cl) for each rock sample.

# References

Anjar, J., Akçar, N., Larsen, E.A., Lyså, A., Marrero, S., Mozafari, N., Vockenhuber, C., 2021. Cosmogenic exposure dating ($^{36}$Cl) of landforms on jan mayen, north Atlantic, and the effects of bedrock formation age assumptions on $^{36}$Cl ages. Geosciences 11, 390. https://doi.org/10.3390/geosciences11090390.

Annell, H., Scoates, J.S., Weis, D., Giret, A., 2007. Petrology of flood basalts at the tholeiitic–alkalic transition and phenocryst compositions, Mt. Marion Dufresne, Kerguelen Archipelago, southern Indian Ocean. Can. Mineral. 45, 809–835. https://doi.org/10.2113/gscanmin.45.4.809.

Bach, E., Radić, V., Schoof, C., 2018. How sensitive are mountain glaciers to climate change? Insights from a block model. J. Glaciol. 64, 247–258. https://doi.org/10.1017/jog.2018.15.

Bakke, J., Paasche, Ø., Schaefer, J.M., Timmermann, A., 2021. Long-term demise of sub-Antarctic glaciers modulated by the Southern Hemisphere Westerlies. Sci. Rep. 11, 8361. https://doi.org/10.1038/s41598-021-87317-5.

Balco, G., Stone, J.O., Lifton, N.A., Dunai, T.J., 2008. A complete and easily accessible means of calculating surface exposure ages or erosion rates from $^{10}$Be and $^{26}$Al measurements. Quat. Geochronol. 3, 174–195. https://doi.org/10.1016/j.quageo.2007.12.001.

Berthier, E., Le Bris, R., Mabileau, L., Testut, L., Rémy, F., 2009. Ice wastage on the kerguelen islands (49 S, 69 E) between 1963 and 2006. J. Geophys. Res.: Earth Surf. 114 https://doi.org/10.1029/2008JF001192.

Chambers, F.M., Brain, S.A., Mauquoy, D., McCarroll, J., Daley, T., 2014. The 'Little Ice Age' in the Southern Hemisphere in the context of the last 3000 years: Peat-based proxy-climate data from Tierra del Fuego. Holocene 24, 1649–1656. https://doi.org/10.1177/0959683614551232.

Charton, J., Jomelli, V., Schimmelpfennig, I., Verfaillie, D., Favier, V., Mokadem, F., Gilbert, A., Brun, F., Aumaitre, G., Bourlès, D.L., 2020. A debris-covered glacier at Kerguelen (49 S, 69 E) over the past 15 000 years. Antarct. Sci. 33, 103–115. https://doi.org/10.1017/S0954102020000541.

Charton, J., Schimmelpfennig, I., Jomelli, V., Delpech, G., Blard, P.-H., Braucher, R., Verfaillie, D., Favier, V., Rinterknecht, V., Goosse, H., 2022. New cosmogenic nuclide constraints on late glacial and Holocene glacier fluctuations in the sub-Antarctic Indian ocean (Kerguelen islands, 49° S). Quat. Sci. Rev. 283, 107461 https://doi.org/10.1016/j.quascirev.2022.107461.

Charton, J., Schimmelpfennig, I., Jomelli, V., Verfaillie, D., Delpech, G., Guillaume, D., Favier, V., Menviel, L., Robert, T., Rinterknecht, V., Legentil, C., A.S.T.E.R. Team, 2024. Late Pleistocene glaciations on the sub-Antarctic Kerguelen Archipelago: new evidence from $^{36}$Cl CRE dating and comparison with other southern mid-latitude glacier records. Quat. Sci. Rev. 328, 108533 https://doi.org/10.1016/j.quascirev.2024.108533.

Civel-Mazens, M., Crosta, X., Cortese, G., Michel, E., Mazaud, A., Ther, O., Ikehara, M., Itaki, T., 2021. Antarctic polar front migrations in the kerguelen plateau region, Southern Ocean, over the past 360 kyrs. Global Planet. Change 202, 103526. https://doi.org/10.1016/j.gloplacha.2021.103526.

Cook, A.J., Vaughan, D.G., Luckman, A.J., Murray, T., 2014. A new Antarctic Peninsula glacier basin inventory and observed area changes since the 1940s. Antarct. Sci. 26, 614–624. https://doi.org/10.1017/S0954102014000200.

Darvill, C.M., 2013. Cosmogenic nuclide analysis. In: Clarke, L., Nield, J. (Eds.), Geomorphological Techniques. British Society for Geomorphology. London.

Deline, P., Linge, H., Ravanel, L., Tuestad, T., Lafite, R., Bakke, J., Arnaud, F., 2024. Mapping of morainic complexes and reconstruction of glacier dynamics north-east of Cook Ice Cap, Kerguelen Archipelago (49°S). Antarct. Sci. 1–26. https://doi.org/10.1017/S0954102023000378.

Favier, V., Verfaillie, D., Berthier, E., Menegoz, M., Jomelli, V., Kay, J., Ducret, L., Malbéteau, Y., Brunstein, D., Gallée, H., 2016. Atmospheric drying as the main driver of dramatic glacier wastage in the southern Indian Ocean. Sci. Rep. 6, 32396 https://doi.org/10.1038/srep32396.

Fogt, R.L., Marshall, G.J., 2020. The southern annular Mode: variability, trends, and climate impacts across the southern Hemisphere. Wiley Interdisciplinary Reviews: Clim. Change 11, e652. https://doi.org/10.1002/wcc.652.

Frenot, Y., Gloaguen, J., Picot, G., Bougère, J., Benjamin, D., 1993. Azorella selago Hook. used to estimate glacier fluctuations and climatic history in the Kerguelen Islands over the last two centuries. Oecologia 95, 140–144. https://doi.org/10.1016/S0764-4469(97)84712-9.

Frenot, Y., Gloaguen, J.-C., Van De Vijver, B., Beyens, L., 1997. Datation de quelques sédiments tourbeux holocènes et oscillations glaciaires aux îles Kerguelen. Compt. Rendus Acad. Sci. III Sci. Vie. 320, 567–573.

Gautier, I., Weis, D., Mennessier, J.-P., Vidal, P., Giret, A., Loubet, M., 1990. Petrology and geochemistry of the Kerguelen Archipelago basalts (South Indian Ocean): evolution of the mantle sources from ridge to intraplate position. Earth Planet Sci. Lett. 100, 59–76. https://doi.org/10.1016/0012-821X(90)90176-X.

Gordon, J.E., Haynes, V.M., Hubbard, A., 2008. Recent glacier changes and climate trends on South Georgia. Global Planet. Change 60, 72–84.

Hall, K., 1984. Evidence in favour of an extensive ice cover on sub-Antarctic Kerguelen Island during the last glacial. Palaeogeogr. Palaeoclimatol. Palaeoecol. 47, 225–232.

Hodgson, D.A., Graham, A.G., Roberts, S.J., Bentley, M.J., Cofaigh, C.Ó., Verleyen, E., Vyverman, W., Jomelli, V., Favier, V., Brunstein, D., 2014. Terrestrial and submarine evidence for the extent and timing of the Last Glacial Maximum and the onset of deglaciation on the maritime-Antarctic and sub-Antarctic islands. Quat. Sci. Rev. 100, 137–158. https://doi.org/10.1016/j.quascirev.2013.12.001.

Hodgson, D.A., Sime, L.C., 2010. Southern westerlies and CO2. Nat. Geosci. 3, 666–667. https://doi.org/10.1038/ngeo970.

Ivy-Ochs, S., Kerschner, H., Maisch, M., Christl, M., Kubik, P.W., Schlüchter, C., 2009. Latest pleistocene and Holocene glacier variations in the European alps. Quat. Sci. Rev. 28, 2137–2149. https://doi.org/10.1016/j.quascirev.2009.03.009.

Jomelli, V., Mokadem, F., Schimmelpfennig, I., Chapron, E., Rinterknecht, V., Favier, V., Verfaillie, D., Brunstein, D., Legentil, C., Michel, E., 2017. Sub-Antarctic glacier extensions in the Kerguelen region (49 S, Indian Ocean) over the past 24,000 years constrained by ³⁶Cl moraine dating. Quat. Sci. Rev. 162, 128–144. https://doi.org/10.1016/j.quascirev.2017.03.010.

Jomelli, V., Schimmelpfennig, I., Favier, V., Mokadem, F., Landais, A., Rinterknecht, V., Brunstein, D., Verfaillie, D., Legentil, C., Aumaitre, G., 2018. Glacier extent in sub-Antarctic Kerguelen archipelago from MIS 3 period: evidence from ³⁶Cl dating. Quat. Sci. Rev. 183, 110–123. https://doi.org/10.1016/j.quascirev.2018.01.008.

Kaplan, M.R., Schaefer, J., Strelin, J.A., Denton, G., Anderson, R., Vandergoes, M., Finkel, R., Schwartz, R., Travis, S., Garcia, J., 2016. Patagonian and southern south Atlantic view of Holocene climate. Quat. Sci. Rev. 141, 112–125. https://doi.org/10.1016/j.quascirev.2016.03.014.

Kaplan, M.R., Schaefer, J.M., Denton, G.H., Doughty, A.M., Barrell, D.J., Chinn, T.J., Putnam, A.E., Andersen, B.G., Mackintosh, A., Finkel, R.C., 2013. The anatomy of long-term warming since 15 ka in New Zealand based on net glacier snowline rise. Geology 41, 887–890. https://doi.org/10.1130/G34288.1.

Le Maitre, R.W., 1989. A Classification of Igneous Rocks and Glossary of Terms, Recommendations of the International Union of Geological Sciences Subcommission on the Systematics of Igneous Rocks. Blackwell Scientific, Oxford, p. 40.

Le Quéré, C., Rödenbeck, C., Buitenhuis, E.T., Conway, T.J., Langenfelds, R., Gomez, A., Labuschagne, C., Ramonet, M., Nakazawa, T., Metzl, N., Gillett, N., Heimann, M., 2007. Saturation of the Southern OceanOcean CO₂ sink due to recent climate change. Science 316, 1735–1738. https://doi.org/10.1126/science.1136188.

Lifton, N., Sato, T., Dunai, T.J., 2014. Scaling in situ cosmogenic nuclide production rates using analytical approximations to atmospheric cosmic-ray fluxes. Earth Planet Sci. Lett. 386, 149–160. https://doi.org/10.1016/j.epsl.2013.10.052.

Marrero, S.M., Phillips, F.M., Borchers, B., Lifton, N., Aumer, A., Balco, G., 2016a. Cosmogenic nuclide systematics and the CRONUScalc program. Quat. Geochronol. 31, 160–187. https://doi.org/10.1016/j.quageo.2015.09.005.

Marrero, S.M., Phillips, F.M., Caffee, M.W., Gosse, J.C., 2016b. CRONUS-Earth cosmogenic 36Cl calibration. Quat. Geochronol. 31, 199–219. https://doi.org/10.1016/j.quageo.2015.10.002.

Marrero, S.M., Phillips, F.M., Caffee, M., Gosse, J., 2021. Corrigendum to "CRONUS-Earth cosmogenic ³⁶Cl calibration", 2016b Quat. Geochronol. 31, 199–219. https://doi.org/10.1016/j.quageo.2020.101130. Quaternary Geochronology 61, 101130.

Masarik, J., Wieler, R., 2003. Production rates of cosmogenic nuclides in boulders. Earth Planet Sci. Lett. 216, 201–208. https://doi.org/10.1016/S0012-821X(03)00476-X.

Mendelová, M., Hein, A.S., Rodés, Á., Smedley, R.K., Xu, S., 2020. Glacier expansion in central Patagonia during the Antarctic Cold Reversal followed by retreat and stabilisation during the Younger Dryas. Quat. Sci. Rev. 227, 106047. https://doi.org/10.1016/j.quascirev.2019.106047.

Moreno, P.I., Vilanova, I., Villa-Martínez, R., Garreaud, R., Rojas, M., De Pol-Holz, R., 2018. Southern Annular Mode-like changes in southwestern Patagonia at centennial timescales over the last three millennia. Nat. Commun. 5, 4375. https://doi.org/10.1038/ncomms5375.

Mulvaney, R., Abram, N.J., Hindmarsh, R.C., Arrowsmith, C., Fleet, L., Triest, J., Sime, L.C., Alemany, O., Foord, S., 2012. Recent Antarctic Peninsula warming relative to Holocene climate and ice-shelf history. Nature 489, 141–144. https://doi.org/10.1038/nature11391.

Murray, D.S., Carlson, A.E., Singer, B.S., Anslow, F.S., He, F., Caffee, M., Marcott, S.A., Liu, Z., Otto-Bliesner, B.L., 2012. Northern Hemisphere forcing of the last deglaciation in southern Patagonia. Geology 40, 631–634. https://doi.org/10.1130/G32836.1.

Neukom, R., Gergis, J., Karoly, D.J., Wanner, H., Curran, M., Elbert, J., González-Rouco, F., Linsley, B.K., Moy, A.D., Mundo, I., Raible, C.C., Steig, E.J., van Ommen, T., Vance, T., Villalba, R., Zinke, J., Frank, D., 2014. Inter-hemispheric temperature variability over the past millennium. Nat. Clim. Change 4, 362–367. https://doi.org/10.1038/nclimate2174.

Nicolussi, K., Le Roy, M., Schlüchter, C., Stoffel, M., Wacker, L., 2022. The glacier advance at the onset of the Little ice age in the alps: new evidence from Mont miné and morteratsch glaciers. Holocene 32, 624–638. https://doi.org/10.1177/09596836221088247.

Nougier, J., 1970. Aspects de morpho-tectonique glaciaire aux Iles Kerguelen. Rev. Geogr. Phys. Geol. Dyn. 14, 499–505.

Oppedal, L.T., Bakke, J., Paasche, Ø., Werner, J.P., van der Bilt, W.G.M., 2018. Cirque Glacier on South Georgia shows centennial variability over the last 7000 years. Front. Earth Sci. 6 https://doi.org/10.3389/feart.2018.00002.

Orme, L.C., Crosta, X., Miettinen, A., Divine, D.V., Husum, K., Isaksson, E., Wacker, L., Mohan, R., Ther, O., Ikehara, M., 2020. Sea surface temperature in the Indian sector of the Southern Ocean over the late glacial and Holocene. Clim. Past 16, 1451–1467. https://doi.org/10.5194/cp-16-1451-2020.

Parish, T.R., Cassano, J.J., 2003. The role of katabatic winds on the antarctic surface wind regime. Mon. Weather Rev. 131, 317–333. https://doi.org/10.1175/1520-0493(2003)131<0317:TROKWO>2.0.CO;2.

Park, Y.-H., Vivier, F., Roquet, F., Kestenare, E., 2009. Direct observations of the ACC transport across the Kerguelen plateau. Geophys. Res. Lett. 36 https://doi.org/10.1029/2009GL039617.

Petherick, L.M., Knight, J., Shulmeister, J., Bostock, H., Lorrey, A., Fitchett, J., Eaves, S., Vandergoes, M.J., Barrows, T.T., Barrell, D.J.A., Eze, P.N., Hesse, P., Jara, I.A., Mills, S., Newnham, R., Pedro, J., Ryan, M., Saunders, K.M., White, D., Rojas, M., Turney, C., 2022. An extended last glacial maximum in the Southern Hemisphere: a contribution to the SHeMax project. Earth Sci. Rev. 231, 104090 https://doi.org/10.1016/j.earscirev.2022.104090.

Phillips, F.M., Stone, W.D., Fabryka-Martin, J.T., 2001. An improved approach to calculating low-energy cosmic-ray neutron fluxes near the land/atmosphere interface. Chem. Geol. 175, 689–701. https://doi.org/10.1016/S0009-2541(00)00329-6.

Putnam, A.E., Denton, G.H., Schaefer, J.M., Barrell, D.J.A., Andersen, B.G., Finkel, R.C., Schwartz, R., Doughty, A.M., Kaplan, M.R., Schlüchter, C., 2010. Glacier advance in southern middle-latitudes during the antarctic cold reversal. Nat. Geosci. 3, 700–704. https://doi.org/10.1038/ngeo962.

Rasmussen, S.O., Bigler, M., Blockley, S.P., Blunier, T., Buchardt, S.L., Clausen, H.B., Cvijanovic, I., Dahl-Jensen, D., Johnsen, S.J., Fischer, H., Gkinis, V., Guillevic, M., Hoek, W.Z., Lowe, J.J., Pedro, J.B., Popp, T., Seierstad, I.K., Steffensen, J.P., Svensson, A.M., Vallelonga, P., Vinther, B.M., Walker, M.J.C., Wheatley, J.J., Winstrup, M., 2014. A stratigraphic framework for abrupt climatic changes during the Last Glacial period based on three synchronized Greenland ice-core records: refining and extending the INTIMATE event stratigraphy. Quat. Sci. Rev. 106, 14–28. https://doi.org/10.1016/j.quascirev.2014.09.007.

Renac, C., Kyser, K., Bowden, P., Moine, B., Cottin, J.-Y., 2010. Hydrothermal fluid interaction in basaltic lava units, Kerguelen Archipelago (SW Indian Ocean). Eur. J. Mineral 22, 215–234. https://doi.org/10.1127/0935-1221/2009/0022-1993.

Reynhout, S.A., Sagredo, E.A., Kaplan, M.R., Aravena, J.C., Martini, M.A., Moreno, P.I., Rojas, M., Schwartz, R., Schaefer, J.M., 2019. Holocene glacier fluctuations in Patagonia are modulated by summer insolation intensity and paced by Southern Annular Mode-like variability. Quat. Sci. Rev. 220, 178–187. https://doi.org/10.1016/j.quascirev.2019.05.029.

Rowan, A.V., 2017. The 'Little Ice Age' in the Himalaya: a review of glacier advance driven by Northern Hemisphere temperature change. Holocene 27, 292–308. https://doi.org/10.1177/0959683616658530.

Saunders, K.M., Roberts, S.J., Perren, B., Butz, C., Sime, L., Davies, S., Van Nieuwenhuyze, W., Grosjean, M., Hodgson, D.A., 2018. Holocene dynamics of the Southern Hemisphere westerly winds and possible links to CO2 outgassing. Nat. Geosci. 11, 650–655. https://doi.org/10.1038/s41561-018-0186-5.

Schaefer, J.M., Denton, G.H., Kaplan, M., Putnam, A., Finkel, R.C., Barrell, D.J.A., Andersen, B.G., Schwartz, R., Mackintosh, A., Chinn, T., Schlüchter, C., 2009. High-frequency Holocene glacier fluctuations in New Zealand differ from the northern signature. Science 324, 622–625. https://doi.org/10.1126/science.1169312.

Schimmelpfennig, I., Benedetti, L., Finkel, R., Pik, R., Blard, P.-H., Bourlès, D., Burnard, P., Williams, A., 2009. Sources of in-situ ³⁶Cl in basaltic rocks. Implications for calibration of production rates. Quat. Geochronol. 4, 441–461. https://doi.org/10.1016/j.quageo.2009.06.003.

Schimmelpfennig, I., Benedetti, L., Garreta, V., Pik, R., Blard, P.-H., Burnard, P., Bourles, D., Finkel, R., Ammon, K., Dunai, T., 2011. Calibration of cosmogenic ³⁶Cl production rates from Ca and K spallation in lava flows from Mt. Etna (38 N, Italy) and Payun Matru (36 S, Argentina). Geochem. Cosmochim. Acta 75, 2611–2632.

Schimmelpfennig, I., Schaefer, J., Putnam, A., Koffman, T., Benedetti, L., Ivy-Ochs, S., ASTER Team, Schlüchter, C., 2014. ³⁶Cl production rate from K-spallation in the European Alps (Chironico landslide, Switzerland). J. Quat. Sci. 29, 407–413.

Sigman, D.M., Hain, M.P., Haug, G.H., 2010. The polar ocean and glacial cycles in atmospheric CO2 concentration. Nature 466, 47–55. https://doi.org/10.1038/nature09149.

Solomina, O.N., Bradley, R.S., Hodgson, D.A., Ivy-Ochs, S., Jomelli, V., Mackintosh, A.N., Nesje, A., Owen, L.A., Wanner, H., Wiles, G.C., Young, N.E., 2015. Holocene glacier fluctuations. Quat. Sci. Rev. 111, 9–34. https://doi.org/10.1016/j.quascirev.2014.11.018.

Stone, J., 2000. Air pressure and cosmogenic isotope production. J. Geophys. Res. 105, 23753–23760. https://doi.org/10.1029/2000JB900181.

Strelin, J.A., Denton, G.H., Vandergoes, M.J., Ninnemann, U.S., Putnam, A.E., 2011. Radiocarbon chronology of the late-glacial puerto bandera moraines, southern patagonian Icefield, Argentina. Quat. Sci. Rev. 30, 2551–2569. https://doi.org/10.1016/j.quascirev.2011.05.004.

Strelin, J.A., Kaplan, M.R., Vandergoes, M.J., Denton, G.H., Schaefer, J.M., 2014. Holocene glacier history of the Lago argentino basin, southern patagonian Icefield. Quat. Sci. Rev. 101, 124–145. https://doi.org/10.1016/j.quascirev.2014.06.026.

Tuestad, T., 2023. [Unpublished Raw Bulk Rock Chemical Composition Data]. University of Bergen.

van As, D., Fausto, R.S., Steffen, K., Team, P.P., 2014. Katabatic Winds and Piteraq Storms: Observations from the Greenland Ice Sheet. Geological Survey of Denmark and Greenland Bulletin., pp. 83–86

van der Bilt, W.G.M., Bakke, J., Werner, J.P., Paasche, Ø., Rosqvist, G., Vatle, S.S., 2017. Late Holocene glacier reconstruction reveals retreat behind present limits and two-stage Little Ice Age on subantarctic South Georgia. J. Quat. Sci. 32, 888–901. https://doi.org/10.1002/jqs.2937.

van der Putten, N., Verbruggen, C., Björck, S., Michel, E., Disnar, J.-R., Chapron, E., Moine, B.N., de Beaulieu, J.-L., 2015. The last termination in the South Indian ocean: a unique terrestrial record from kerguelen islands (49°S) situated within the Southern Hemisphere westerly belt. Quat. Sci. Rev. 122, 142–157. https://doi.org/10.1016/j.quascirev.2015.05.010.

Verfaillie, D., Favier, V., Dumont, M., Jomelli, V., Gilbert, A., Brunstein, D., Gallée, H., Rinterknecht, V., Menegoz, M., Frenot, Y., 2015. Recent glacier decline in the Kerguelen Islands (49°S, 69°E) derived from modeling, field observations, and satellite data. J. Geophys. Res.: Earth Surf. 120, 637–654. https://doi.org/10.1002/2014JF003329.

Verfaillie, D., Favier, V., Gallée, H., Fettweis, X., Agosta, C., Jomelli, V., 2019. Regional modeling of surface mass balance on the Cook ice cap, kerguelen islands (49°S, 69°E). Clim. Dynam. 53, 5909–5925. https://doi.org/10.1007/s00382-019-04904-z.

Verfaillie, D., Charton, J., Schimmelpfennig, I., Stroebele, Z., Jomelli, V., Bétard, F., Favier, V., Cavero, J., Berthier, E., Goosse, H., Rinterknecht, V., Legentil, C., Charrassin, R., Aumaître, G., Bourlès, D.L., Keddadouche, K., 2021. Evolution of the Cook Ice Cap (Kerguelen Islands) between the last centuries and 2100 ce based on

cosmogenic dating and glacio-climatic modelling. Antarct. Sci. 33, 301–317. https://doi.org/10.1017/S0954102021000080.

WAIS Divide Project Members, 2013. Onset of deglacial warming in West Antarctica driven by local orbital forcing. Nature 500, 440–444. https://doi.org/10.1038/nature12376.

Walker, M., Gibbard, P., Head, M.J., Berkelhammer, M., Björck, S., Cheng, H., Cwynar, L. C., Fisher, D., Gkinis, V., Long, A., Lowe, J., Newnham, R., Rasmussen, S.O.,

Weiss, H., 2019. Formal subdivision of the Holocene series/epoch: a summary. J. Geol. Soc. India 93, 135–141. https://doi.org/10.1007/s12594-019-1141-9.

Wilcken, K.M., Freeman, S.P.H.T., Schnabel, C., Binnie, S.A., Xu, S., Phillips, R.J., 2013. $^{36}$Cl accelerator mass spectrometry with a bespoke instrument. Nucl. Instrum. Methods Phys. Res. Sect. B Beam Interact. Mater. Atoms 294, 107–114. https://doi.org/10.1016/j.nimb.2012.04.027.